

POLITECNICO DI TORINO

Department of Mechanical and Aerospace Engineering

Master Degree Course in Aerospace Engineering



**Politecnico
di Torino**



UNIVERSITÀ
DEGLI STUDI
FIRENZE



Master's degree Thesis

Comparison between different 3D Flutter Solvers

Supervisors

Prof. Ing. Christian Maria Firrone

Prof. Ing. Daniele Botto

Prof. Ing. Lorenzo Pinelli

Ing. Antonio Giuseppe D'Ettola

Candidate

Stefano Raimondo

Academic Year 2022/2023

Per Aspera ad Astra

Politecnico di Torino, 13 Aprile 2023

Acknowledgment

Un grazie speciale alla mia famiglia, ai miei amici e a tutte le persone che hanno sempre creduto in me!

Abstract

This thesis work, developed in collaboration with AvioAero - A GE Aviation Business, has the goal to analyze the aeroelastic behavior of LPT blade.

Today in fact one of the most important objective of the aerospace industry is to realize lighter engines with a lower environmental impact.

Particularly is object of study an innovative type of blades, realized with a new geometry and lighter materials, which could manifest aeroelastic instabilities during the flight mission. This thesis work in fact is the result of a collaboration with the ARIAS project, which is an European project which studies aeroelasticity stability and forced response on a tip free type of blades with a wide choice of configurations.

A detailed 3D Flutter Analysis, which is a multidisciplinary work that includes both fluid-dynamics and structural analysis, could strongly help the designers to better understand the aeroelastic response of this new generation of blades.

Contents

| | |
|---|----|
| 1. Introduction..... | 1 |
| 1.1 Aircraft engines..... | 1 |
| 4.3 Turbofan..... | 3 |
| 4.3 Turboshaft..... | 5 |
| 1.4 Turboprop..... | 6 |
| 2. Rotor Dynamics..... | 8 |
| 2.1 Rotor dynamics and cyclic symmetry..... | 10 |
| 2.2 Modal analysis..... | 12 |
| 2.3 Modal analysis using cyclic symmetry..... | 17 |
| 2.4 Modal assurance criterion (MAC)..... | 19 |
| 2.5 Forced Response..... | 21 |
| 3. Aeroelasticity in turbomachinery..... | 27 |
| 3.1 Aircraft engine aeroelasticity..... | 30 |
| 3.2 Flutter stability..... | 34 |
| 3.2 Classification of flutter..... | 35 |
| 4. 3D Flutter Analysis..... | 36 |
| 4.1 The ARIAS project..... | 36 |
| 4.2 Numerical setup..... | 42 |
| 4.3 Sensitivity around the operational point..... | 58 |
| 4.4 Sensitivity around the configuration..... | 74 |
| 4.5 Sensitivity around the solvers..... | 83 |

| | |
|-------------------------------|----|
| 5. Conclusions..... | 86 |
| 5.1 Future developments | 87 |
| 6. References..... | 90 |

List of Figures

| | |
|---|----|
| Figure 1: The ETDC..... | 1 |
| Figure 2: Bryaton-Joule cycle..... | 2 |
| Figure 3: GE 9X..... | 4 |
| Figure 4: GE T901..... | 5 |
| Figure 5: GE Catalyst..... | 6 |
| Figure 6: Axial turbine stage..... | 8 |
| Figure 7: Turbine sectors model..... | 10 |
| Figure 8: 1 Nodal diameter..... | 12 |
| Figure 9: 2 Nodal diameters..... | 13 |
| Figure 10: Examples of some modes..... | 14 |
| Figure 11: Frequency-Nodal diameters diagram..... | 15 |
| Figure 12: Theoretical FreND diagram..... | 16 |
| Figure 13: Fundamental sector..... | 17 |
| Figure 14: The MAC..... | 20 |
| Figure 15: Aerodynamic force..... | 21 |
| Figure 16: Example of Engine Order..... | 22 |
| Figure 17: Two sectors..... | 22 |

| | |
|--|----|
| Figure 18: Campbell diagram..... | 23 |
| Figure 19: Experimental Campbell diagram..... | 24 |
| Figure 20: Zig – Zag diagram: N even..... | 25 |
| Figure 21: Zig – Zag diagram N odd..... | 26 |
| Figure 22: Collar diagram..... | 27 |
| Figure 23: Flutter vibrations on Campbell diagram..... | 28 |
| Figure 24: Tacoma Narrows bridge..... | 29 |
| Figure 25: Flutter damage in a steam turbine..... | 30 |
| Figure 26: LPT CFD analysis..... | 31 |
| Figure 27: Modal analysis..... | 32 |
| Figure 28: Coupled flutter..... | 33 |
| Figure 29: Classification of flutter..... | 35 |
| Figure 30: ARIAS partners..... | 37 |
| Figure 31: CTA rig..... | 37 |
| Figure 32: ARIAS cold flow bladed disk..... | 38 |
| Figure 33: Some configurations..... | 39 |
| Figure 34: FEM model of the disk..... | 40 |
| Figure 35: FEM model of the blade..... | 41 |
| Figure 36: M 1, ND 2: Sideview..... | 43 |

| | |
|-------------------------------------|----|
| Figure 37: M 1, ND 2: Topview..... | 43 |
| Figure 38: M 2, ND 2: Sideview..... | 44 |
| Figure 39: M 2, ND 2: Topview..... | 44 |
| Figure 40: M 3, ND 2: Sideview..... | 45 |
| Figure 41: M 3, ND 2: Topview..... | 45 |
| Figure 42: M 1, ND 4: Sideview..... | 46 |
| Figure 43: M 1, ND 4: Topview..... | 46 |
| Figure 44: M 2, ND 4: Sideview..... | 47 |
| Figure 45: M 2, ND 4: Topview..... | 47 |
| Figure 46: M 3, ND 4: Sideview..... | 48 |
| Figure 47: M 3, ND 4: Topview..... | 48 |
| Figure 48: M 1, ND 8: Sideview..... | 49 |
| Figure 49: M 1, ND 8: Topview..... | 49 |
| Figure 50: M 2, ND 8: Sideview..... | 50 |
| Figure 51: M 2, ND 8: Topview..... | 50 |
| Figure 52: M 3, ND 8: Sideview..... | 51 |
| Figure 53: M 3, ND 8: Topview..... | 51 |
| Figure 54: Mid-span mesh..... | 53 |
| Figure 55: Pressure field..... | 54 |

| | |
|--|----|
| Figure 56: Streamlines..... | 54 |
| Figure 57: Flutter report..... | 57 |
| Figure 58: Blade A1D1..... | 58 |
| Figure 59: A1D1 FEM model..... | 58 |
| Figure 60: Mode 1..... | 59 |
| Figure 61: Mode 2..... | 59 |
| Figure 62: FreND A1D1 103 % RPM..... | 60 |
| Figure 63: Convergence 103 % RPM..... | 61 |
| Figure 64: Inlet and Outlet 103 % RPM..... | 61 |
| Figure 65: Mach and Pressure 103 % RPM..... | 62 |
| Figure 66: Aerodamping A1D1 103 % RPM: Mode 1..... | 62 |
| Figure 67: Aerodamping A1D1 103 % RPM: Mode 2..... | 63 |
| Figure 68: FreND A1D1 90 % RPM..... | 64 |
| Figure 69: Convergence 90 % RPM..... | 65 |
| Figure 70: Inlet and Outlet 90 % RPM..... | 66 |
| Figure 71: Mach and Pressure 90 % RPM..... | 66 |
| Figure 72: Aerodamping A1D1 90 % RPM: Mode 1..... | 66 |
| Figure 73: Aerodamping A1D1 90% RPM: Mode 2..... | 67 |
| Figure 74: FreND A1D1 62 % RPM..... | 68 |

| | |
|---|----|
| Figure 75: Convergence 62 % RPM..... | 69 |
| Figure 76: Inlet and Outlet 62 % RPM..... | 69 |
| Figure 77: Mach and Pressure 62 % RPM..... | 70 |
| Figure 78: Aerodamping A1D1 62 % RPM: Mode 1..... | 70 |
| Figure 79: Aerodamping A1D1 62 % RPM: Mode 2..... | 71 |
| Figure 80: Aerodamping A1D1 Mode 1: Comparison with rotational speed..... | 72 |
| Figure 81: Aerodamping A1D1 Mode 2: Comparison with rotational speed..... | 72 |
| Figure 82: Under – platform steel damper..... | 74 |
| Figure 83: Damper FEM model..... | 74 |
| Figure 84: FreND A1SD 103 % RPM..... | 75 |
| Figure 85: Aerodamping A1SD 103 % RPM: Mode 1..... | 76 |
| Figure 86: Aerodamping A1SD 103 % RPM: Mode 2..... | 76 |
| Figure 87: FreND A1SD 62 % RPM..... | 77 |
| Figure 88: Aerodamping A1SD 62 % RPM: Mode 1..... | 78 |
| Figure 89: Aerodamping A1SD 62 % RPM: Mode 2..... | 78 |
| Figure 90: Aerodamping A1SD Mode 1: Comparison with rotational speed..... | 79 |
| Figure 91: Aerodamping: A1D1 vs A1SD..... | 80 |
| Figure 92: A1SD: Critical nodal diameter..... | 81 |
| Figure 93: Density of aerodynamic work..... | 81 |

| | |
|---|----|
| Figure 94: CFD analysis 103 % RPM: Pressure field..... | 83 |
| Figure 95: CFD analysis 62 % RPM: Pressure field..... | 83 |
| Figure 96: A1D1 Mode 2 103 % RPM: Linearized vs Non – Linearized..... | 84 |
| Figure 97: A1D1 Mode 2 62 % RPM: Linearized vs Non – Linearized..... | 85 |
| Figure 98: Double blade configuration..... | 87 |
| Figure 99: Mode 1 and Mode 2..... | 88 |
| Figure 100: Aerodamping A1C2 – A1: Mode 1and Mode 2..... | 89 |

Chapter 1

Introduction

1.1 Aircraft engines

The E-TCDs, European Technology Development Clusters, launched in May 2020, is a network operating into the research and innovation field, with a unique model in Europe, whose members work together under one single framework agreement which defines financial provisions, Ip rules, dissemination and publications. The E-TCDs include up today 33 parties: 22 research institutions, 3 SMEs and 8 GE affiliates. The E-TCDs include 10 different clusters, consisting of research institutions and GE Aviation teams, each of them focused on dedicated disciplines or product of GE Aviation interest.



Figure 1: The ETDC [9]

This thesis work is the result of a collaboration period between GE AvioAero and Polytechnic University of Turin. Particularly It has been studied the interaction between fluid and structure in a Low-Pressure section of an aircraft engine. The goal of the work was specifically the study of the turbine blades flutter behavior. Before describing in detail this phenomenon, in this first chapter will be illustrated the types of aircraft engines that are present nowadays on the market.

First of all it is necessary to say that all of the classical airbreathing engines operate a Brayton-Joule cycle, but every type of engine “uses” this cycle in a different way.

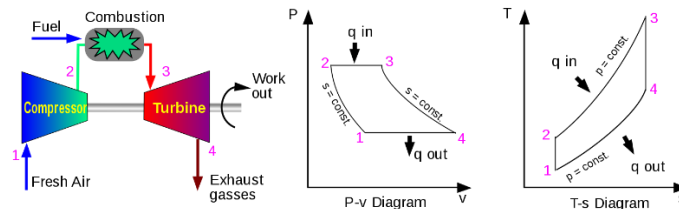


Figure 2: Bryaton-Joule Cycle [16]

Shortly in this type of cycle a gas is compressed and heated after the admission of fuel in the combustion zone, then it passes in the turbines, where it generates mechanical works, then it goes to the nozzle where it is strongly accelerated and produces thrust.

What it has just explained is the typical way of working of a turbofan/turbojet, in which the turbine has just the role to extracts work from the fluid to drive the compressor, then the fluid is sent to the nozzle where the enthalpy is converted into thrust. It is use to say that these types of machines work on a “operational line”, because the power extract from the turbine equals exactly the power needed to drive the compressor. The turboshaft, instead, uses the Brayton-Joule cycle to extract work from the fluid and next use it to drive the compressor and a user. Finally the turboprop is an hybrid of the two configurations explained before, because it uses the fluid both to generate thrust in the nozzle expansion and also to drive a propeller.

4.3 Turbofan

The turbofan is a type of engine which has the task to generate thrust to permit the aircraft flying. Derived from the turbojet, this type of engine is characterized by two different flows: the *cold flow*, which passes only through the fan and then goes to a dedicated nozzle and the *hot flow*, which passes through all the compressor's stages, the combustion zone, expands in the turbines and then goes to his nozzle.

We can define the *ByPass Ratio*:

$$BPR = \frac{\dot{m}_c}{\dot{m}_h} \quad (1.1)$$

where \dot{m}_c is the *cold flow* and \dot{m}_h is the *hot flow*.

Today's the major part of the thrust is product by the cold flow. A good engine has a cold flow with a high *propulsion efficiency* and a hot flow with a high *thermal efficiency*.

It is possible to define the *propulsion efficiency* as:

$$\eta_p = \frac{P_t}{P_t + P_d} = \frac{2}{1 + \frac{v_g}{v_0}} \quad (1.2)$$

where P_t is the power of the thrust, P_d is the power dissipated, v_g is the velocity of the gasses and v_0 is the velocity of the aircraft.

The thermal efficiency is:

$$\eta_{th} = \frac{P_k}{P_{ch}} \quad (1.3)$$

where P_k is the kinetic power and P_{ch} is the "chemistry power", or rather the power contained in the fuel.

We can define the global efficiency as:

$$\eta_g = \eta_p \eta_{th} \quad (1.4)$$

The GE9X represents the *state of the art* of this category of engines: it has an $OPR \approx 60$ and a $BPR \approx 9.9$. It is a double spool engine, with 1 fan stage, 3 booster stages and 11 stages for the high-pressure compressor. Then there are 2 stages for the high-pressure turbine and 6 stages for the low pressure turbine.

This engine will equip the next generation of Boeing 777.

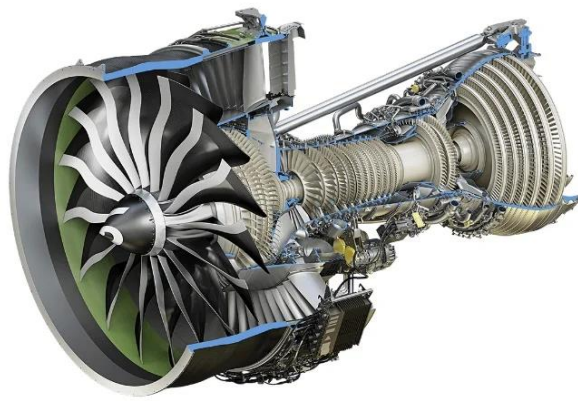


Figure 3: GE 9X [13]

4.3 Turboshaft

Another type of airbreathing engine is the turboshaft which, instead the turbofan which ha the role to produce thrust, it has the role to product mechanical work, which will be used by a user, for example a propeller or a rotor. The goal of this type of engine is to extract work from the fluid in the turbine stages and the use it to drive the compressor and the user. Nowadays the most part of turboshafts are double spool machines with free turbine for power, which has the role to drive just the user. This choice is made to optimize the operation in off design conditions.

An example of this type of engines is the GE T901, 5hich represent the maximum level of the turboshaft technologies. To maximize the reactivity of the engine the designers decided to use a single spool architecture, with a large use of ceramic materials and additive manufacturing technologies. In the future this engine will equip the most advanced fighting helicopters.

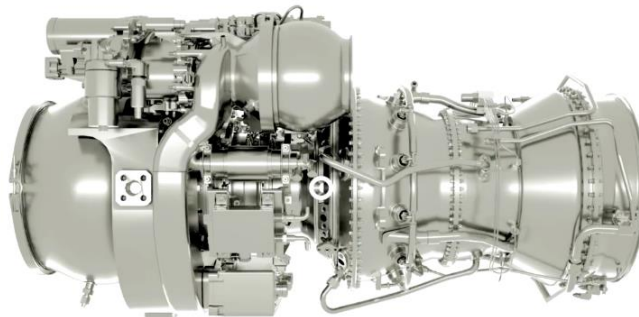


Figure 4: GE T901 [15]

1.4 Turboprop

The turboprop is a combination of the two engine technologies explained before, because the total thrust is the sum of the thrust produced by the propeller driven by the shaft and the ones obtained by the exhaust gasses accelerated by the nozzle. It's possible to write:

$$T_{total} = T_p + T_j \quad (1.4)$$

where T_p is the thrust associated to the propeller and T_j is the contribution of the jet.

An example of this type of technology is the GE Catalyst, which represent the highest level of performances available on the market of turboprops.

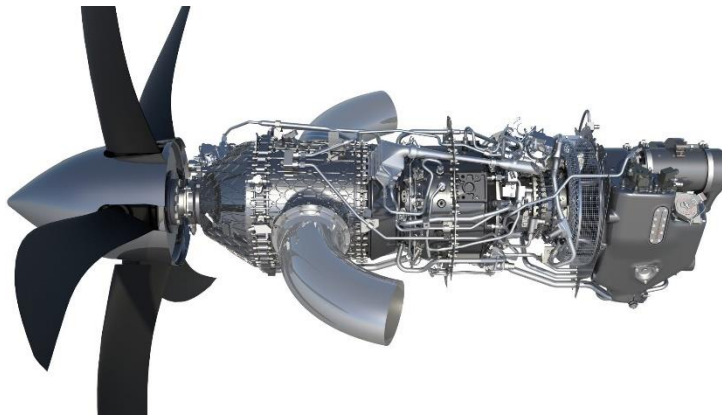


Figure 5: GE Catalyst [17]

The air enters in the engine from the inlet (on the right in the figure above) and then passes through 4 stages of axial compressor and 1 stage of centrifugal compressor. The combustion chamber is a “reverse flow” type: this is typical for turboprops engines, specially to limit the length of its structure. Then the flows goes to 2 stages of High Pressure Turbine (HPT) and then to 3 stages of Low Pressure Turbine (LPT), which drives the propeller. This engine is a typical example of a double shaft machine with a free power turbine.

After this stage the exhaust comes out from the two big tubes placed just behind the gearbox (on the left in the figure above).

This type of machine is characterized by an elevated propulsion efficiency, which theoretically reaches the maximum when the exhaust velocity is equal to the aircraft velocity. The only problem of this technology is the limitation on the flight Mach number ($M_{max} = 0.6$), due to the presence of shock waves at the tip of the propeller's blades. To overcome this problem, CFM, a joint venture between GE Aviation and Safran, is developing a new open rotor engine called RISE, which has an innovative design for supersonic blades, a great bypass ratio, a high level of thrust produced. So this type of machine will combine the technology and advantages of Turbofans and Turboprops and it'll strongly reduce the fuel consumption. This technology will probably be equipped by the next generation of narrow body aircrafts.

The GE Catalyst will equip the next generation of fighting drones.

In the next chapters of this work we will focus the attention on the structural analysis of the Low Pressure Turbine area of the engine, particularly on the problems related to the interaction between fluid and machine.

In particular in the Chapter 2 there will be presented the most important theoretical aspects of the rotor dynamics theory. Next in Chapter 3 will be proposed the basis of the aeroelasticity theory, especially in turbomachinery applications. Then in Chapter 4 will be presented all the studies done on the ARIAS blade, with the sensitivity around the operational point, around the configuration and around the solver.

Chapter 2

Rotor Dynamics

After the general introduction made in the previous chapter, now it's time to focus our attention on the Low Pressure zone of the engine, particularly on the LPT.

First of all it's necessary to introduce the *spool*, which is the sum of a shaft plus a series of bladed disks putted on it. A bladed disk is just a steel disk on which are fitted a series of blades on it.

In this work we will analyze the interaction between the exhaust and a Low Pressure Turbine stage.

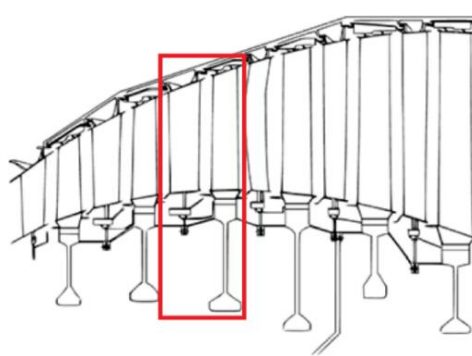


Figure 6: Axial turbine stage

In the picture above is possible to see a typical stage of a Low Pressure Turbine stage, which is made by two different components: the *nozzle*, which is modelled as a convergent duct and has the role to strongly accelerated the flows, and the *rotor*, which has to extract mechanical work from the fluid and transfers it to the shaft. The *nozzle* is connected to the case of the engine, while the rotor blade is fitted on the disk.

Now let's introduce some terminology about a rotor blade:

- *Tip Shroud*: is on the top of the blade and has different roles, such as to limit the generation of whirling structures on the blade's tip and primarily to dump the structure's vibrations.
- *Airfoil*: it represents the surface on where the fluid "works" and transfers motion to the shaft.
- *Shank*: it's the linkage between the airfoil and the part anchored to the disk.
- *Dove tail*: it's the lower part of the blade and it links it to the disk. It can have a different number of lobes.

2.1 Rotor dynamics and cyclic symmetry

In this section will be analyzed what today is essentially to de design of bladed disks, that is the Computational Structural Analysis (CSD) applied to rotating parts.

First of all is necessary to decompose the all system (blade + disk) in a series of singles blocks which they are in contact with they each other. This is the result:

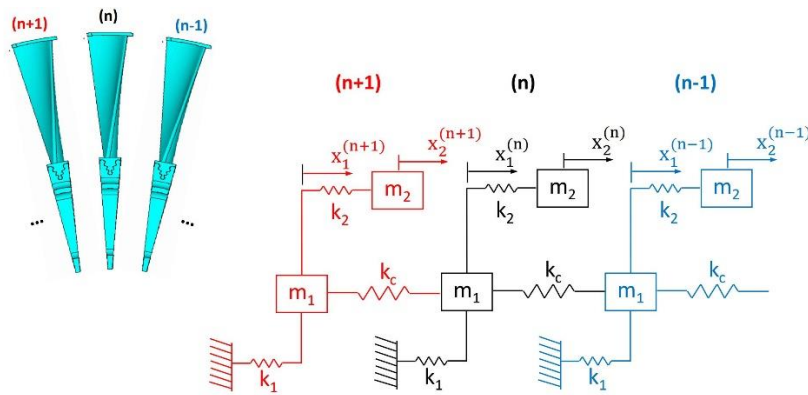


Figure 7: Turbine sectors model [7]

This approach, in which the z axis is the machine axis and the x axis is radial axis is called *cyclic simmetry*. In this first analysis we will consider every sector perfect equal all the other, so we are in a *tuned* system. The behavior of a *mistuned* system, in wich the are differences between the sectors, will be analyzed in the next chapters, in which will be studied the modal and the aeroelastic response of that type of systems.

The fundamental equation of motion for a solid in cyclic simmetry, without dampers and external excitations, assumes this formulation:

$$[M]\{\ddot{x}\} + [K]\{x\} = 0 \quad (2.1)$$

where $[M]$ is the *mass matrix* and $[K]$ is the *stiffness matrix*.

The first one has the typical form of a *block diagonal matrix*:

$$[M] = \begin{bmatrix} m^{(1)} & 0 & \cdots & \cdots & \cdots & \cdots & 0 \\ 0 & m^{(2)} & \cdots & \cdots & \cdots & \cdots & 0 \\ \vdots & \vdots & m^{(3)} & \cdots & \cdots & \cdots & 0 \\ \vdots & \vdots & \vdots & \ddots & \cdots & \cdots & 0 \\ \vdots & \vdots & \vdots & \vdots & \ddots & \cdots & 0 \\ \vdots & \vdots & \vdots & \vdots & \vdots & m^{(N-1)} & 0 \\ 0 & 0 & 0 & 0 & 0 & 0 & m^{(N)} \end{bmatrix}$$

while the second, due to the presence of the contact stiffness between two adjacent sectors, is a *block circulant matrix*:

$$[K] = \begin{bmatrix} k^{(1)} & k_c^{(1)} & 0 & \cdots & \cdots & \cdots & \cdots & \cdots & k_c^{(1)} \\ k_c^{(2)} & k^{(2)} & k_c^{(2)} & 0 & \cdots & \cdots & \cdots & \cdots & 0 \\ 0 & k_c^{(3)} & k_3 & k_c^{(3)} & \cdots & \cdots & \cdots & \cdots & 0 \\ \vdots & \vdots & \vdots & \vdots & \ddots & \cdots & \cdots & \cdots & 0 \\ \vdots & \vdots & \vdots & k_c^{(n)} & k^{(n)} & k_c^{(n)} & \cdots & \cdots & 0 \\ \vdots & \vdots & \vdots & \vdots & \vdots & \vdots & \ddots & \cdots & 0 \\ \vdots & \ddots & 0 \\ 0 & \vdots & \vdots & \vdots & \vdots & \vdots & k_c^{(N-1)} & k^{(N-1)} & k_c^{(N-1)} \\ k_c^{(N)} & 0 & 0 & 0 & 0 & 0 & 0 & k_c^{(N)} & k^{(N)} \end{bmatrix}$$

2.2 Modal analysis

In this chapter we will focus our attention on the modal analysis of a body studied with cyclic symmetry. First of all it's necessary to display what types of modes are present:

- **Real modes:** characterized by the presence of only one eigenvalue, are typical for the bodies with low mechanical coupling in the row.
In this case the model can be simplified, removing the disk and fixing the blade at the root (blade-only analysis). If the mode is real all the points of the blade vibrates in phase or in counter phase.
- **Complex modes:** characterized by the presence of a complex eigenvalue which is made up by the combination of two real eigenvalues in quadrature. In this case there's a high mechanical coupling between blade and disk, and this one strongly participates to the vibration. Here the mode shape is characterized by a travelling wave which "travels" through the row. According to that, if the mode is complex, there will be some points with zero shift. A line which unites two of those points is called *nodal diameter*.

In the next pictures it's possible to visualize what are nodal diameters.

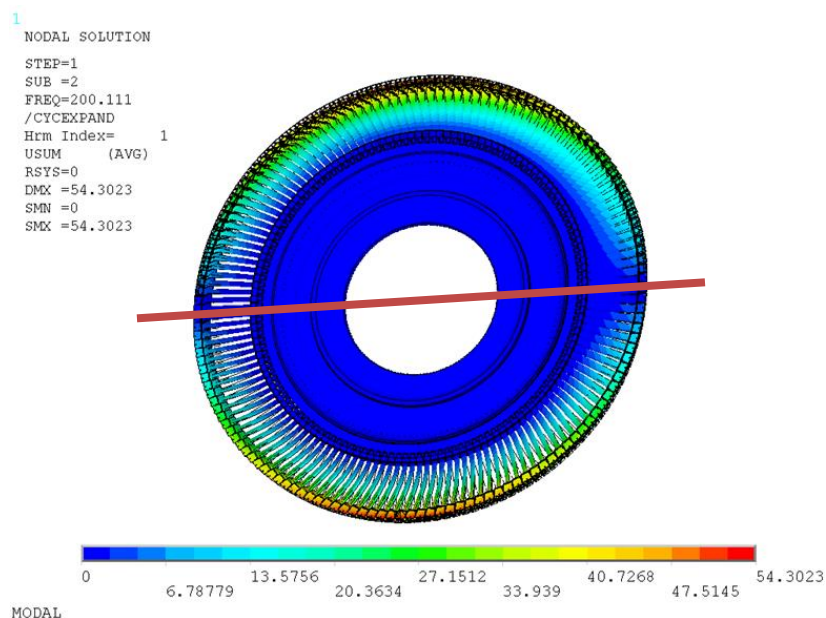


Figure 8: 1 Nodal Diameter

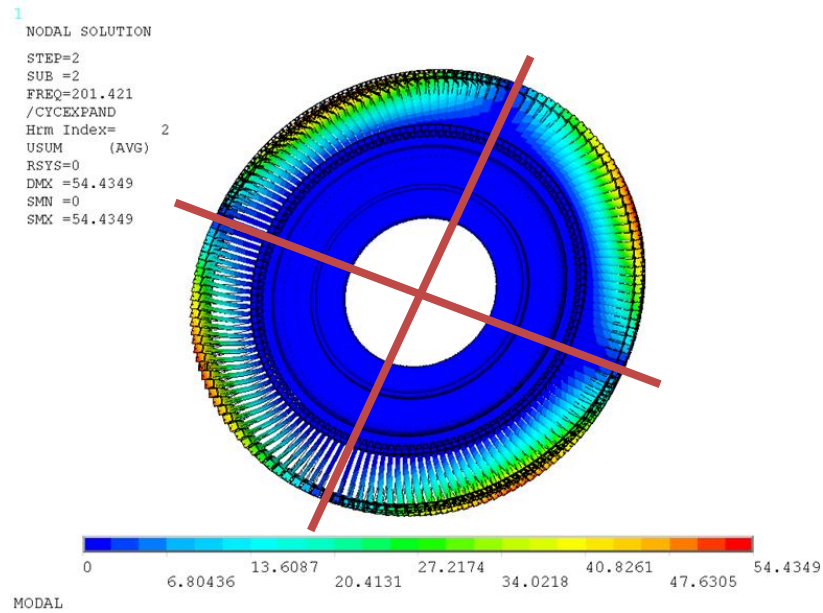


Figure 9: 2 Nodal Diamters

Generally the real modes are considered as a particular case of complex modes.

For a complex mode is possible to write:

$$N\varphi = 2\pi h \quad (2.2)$$

where N is the number of the blades of the row, φ is the Inter Blade Phase Angle (IBPA) and h is the armonic index.

The relationship written above says that for a complex mode every sector vibrates with the same modal form as the adjacent but with a phase displacement.

This phrase could be resumed with this formula:

$$\{\theta^n\} = \{\theta^{n-1}\}e^{j\varphi} = \{\theta^{n-1}\}e^{jh\frac{2\pi}{N}} \quad (2.3)$$

Because the ral modes are a particular case of complex modes we can identify:

- $\varphi = 0$: real mode in which all the blades are moving in phase.
- $\varphi = \pi$: real mode in which all the blades are moving in counter phase.

As it's possible to see in the last page, in a modal analysis of a solid in cyclic symmetry a lot of different type of modes could appear but there's only one fundamental rule that must be respected: a proper mode has to remain the same even after a rigid rotation of an angle equivalent to $\frac{2\pi}{N}$.

In literature is frequent to find also another type of division for the modes:

- **System modes:** in which all the sector participates to the vibration. Usually these types of modes are real modes.
- **Airfoil modes:** in which the zone which vibrates is located in a specific part of the airfoil surface.

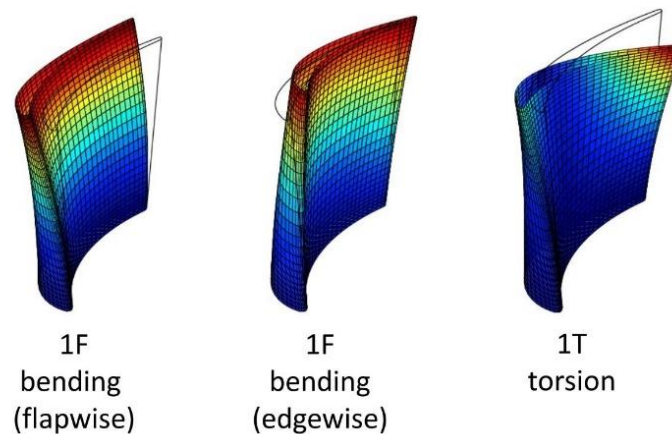


Figure 10: Examples of some modes [4]

Now it's necessary to define which values of IBPA, and also of harmonic indexes, are admitted for complex modes. From equation 2.2 it's possible to write:

$$\varphi = h \frac{2\pi}{N} \quad (2.4)$$

The values of harmonic indexes depend from the number of the blades which compose the row.

N even

$$h = -\frac{N}{2} + 1, -\frac{N}{2} + 2, \dots, -2, -1, 0, 1, 2, \dots, \frac{N}{2} - 2, \frac{N}{2} - 1, \frac{N}{2} \quad (2.5)$$

N odd

$$h = -\frac{N-1}{2}, -\frac{N-1}{2} + 1, \dots, -2, -1, 0, 1, 2, \dots, \frac{N-1}{2} - 1, \frac{N-1}{2} \quad (2.6)$$

At this point we want to understand how the natural frequency associated to a mode could change varying the harmonic index.

Increasing the harmonic index, the number of nodal diameters increases, so in this way it's possible to observe the stiffening of the structure: the natural frequency associated to a specific mode enhances. This phenomena could be see in the so called “*freND*” diagram, in which we can see the behaviour of natural frequencies increasing the nodal diameters.

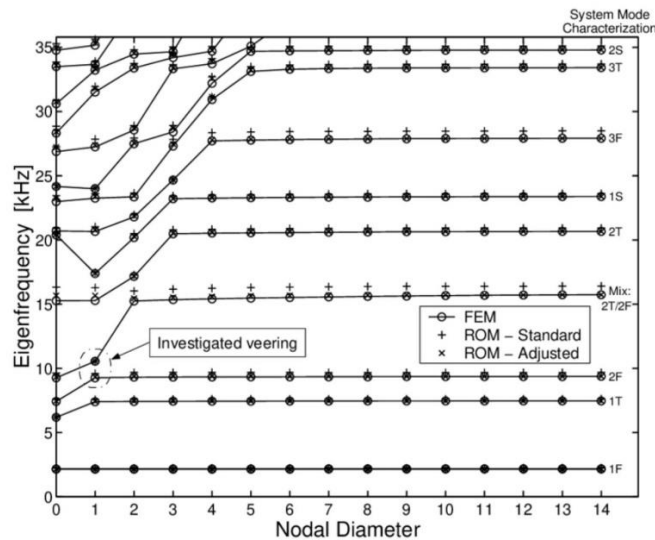


Figure 11: Frequency – Nodal Diameters diagram [21]

In the upper diagram it's possible to observe two interesting behaviours: first of all at high nodal diameters the natural frequency of every modes tends to stabilize

to a precise value. This happens due to the stiffening of the structure, as explained before. Secondly we can see that there's a zone, the *veering* zone, in which the disk's modes strongly interacts with the blade's mode: this is a critical zone, in where the coupled interaction could cause the creation of "dirty" modes.

In follow we can see the theoretical behaviour of the disk's and blade's modes separated:

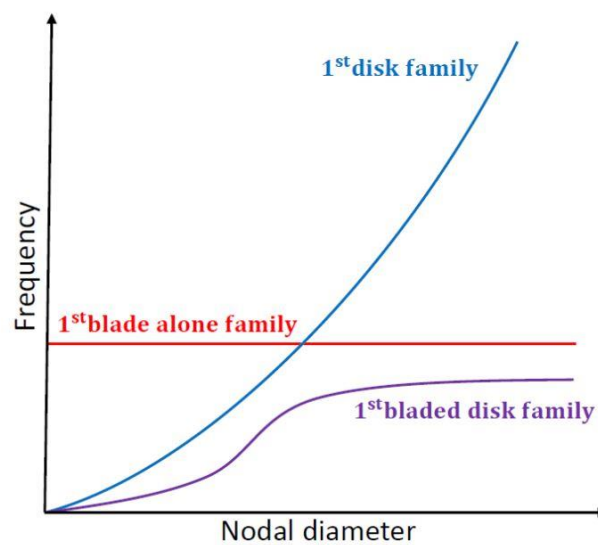


Figure 12: Theoretical FreND diagram [4]

In this graphic is easily to see that behaviours: the blade alone frequency tends to remain constant changing the nodal diameter, while the disk frequency grows monotonous with the nodal diameter. The bladed disk frequency respects the behaviour explained in the page before.

2.3 Modal analysis using cyclic symmetry

In this paragraph is show how to perform a modal analysis witch the cyclic symmetry hypothesis, in the way to reduce the calculation to a single fundamental blade sector.

Let's consider this sector:

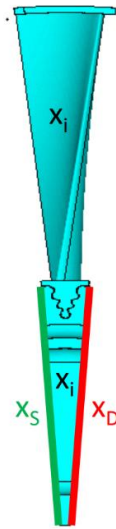


Figure 13: Fundamental sector [7]

where x_i are the internal degrees of freedom, x_s are the degrees of freedom of the left interface and x_d are the degrees of freedom of the right interface. The ineterface degrees of freedom represents the connection of the fundamental sector with the adjacent sectors.

The motion system of equations, before applying the cyclic simmetry, is in this form:

$$(-\omega^2[m^{(n)}] + [k^{(n)}])\{x^{(n)}\} = 0 \quad (2.7)$$

with

$$\{x^{(n)}\} = \begin{Bmatrix} x_d^{(n)} \\ x_i^{(n)} \\ x_s^{(n)} \end{Bmatrix} \quad (2.8)$$

Because the left interface of the n -sector coincides with the left interface of the $n+1$ -sector, it's possible to rewrite the last vector in this form:

$$\{x^{(n)}\} = \begin{Bmatrix} x_d^{(n)} \\ x_i^{(n)} \\ x_d^{(n+1)} \end{Bmatrix} \quad (2.9)$$

Remembering that the boundary conditions for cyclic symmetry are:

$$x_d^{(n+1)} = x_d^{(n)} e^{jh\frac{2\pi}{N}} \quad (2.10)$$

it's possible to define a transformation matrix $[\bar{T}]$ which permits to write the vector $\{x^{(n)}\}$ in this way:

$$\{x^{(n)}\} = \begin{Bmatrix} x_d^{(n)} \\ x_i^{(n)} \\ x_d^{(n+1)} \end{Bmatrix} = \begin{bmatrix} I_d & 0 \\ 0 & I_i \\ I_d e^{jh\frac{2\pi}{N}} & 0 \end{bmatrix} \begin{Bmatrix} x_d^{(n)} \\ x_i^{(n)} \end{Bmatrix} = [\bar{T}] \{x_{SC}^{(n)}\} \quad (2.11)$$

Now applying this transformation to the equation (2.7) the motion system of equations becomes:

$$\left(-\omega^2 [m_{SC}^{(h)}] + [k_{SC}^{(h)}]\right) \{x_{SC}^{(n)}\} = 0 \quad (2.12)$$

where

$$[m_{SC}^{(h)}] = [\bar{T}]^T [m^{(n)}] [\bar{T}] \quad (2.13)$$

and

$$[k_{SC}^{(h)}] = [\bar{T}]^T [k^{(n)}] [\bar{T}] \quad (2.14)$$

2.4 Modal assurance criterion (MAC)

The MAC, *Modal Assurance Calculation*, basically is a number which could be useful to compare the results obtained from two different modal analysis. The difference between the results could come from the model, the technique of solution or if it's used a reduction method, that is the primary reason for which the MAC has been developed in past, when the computers weren't able to perform a complete calculus on a complete solver deck.

The result of this analysis is a scalar number, included between 0 and 1, which comes from a comparison between two vectors, typically displacement vectors.

A MAC number higher than 0.9 is a synonymous of a good match between the vectors.

The MAC is calculated as a normalized scalar product of two vectors, $\{\varphi_X\}$ and $\{\varphi_A\}$ and the results are arranged into the MAC matrix:

$$MAC(r, q) = \frac{|\{\varphi_A\}_r^T \{\varphi_X\}_q|^2}{(\{\varphi_A\}_r^T \{\varphi_A\}_r)(\{\varphi_X\}_r^T \{\varphi_X\}_q)} \quad (2.15)$$

where $\{\varphi_X\}_q$ is the test modal vector, mode q , $\{\varphi_A\}_r$ is the compatyble modal vector, mode r and the apex "T" stands for the operation of transposition.

If the modeshapes are complex is frequently used this notation:

$$MAC(r, q) = \frac{|\{\Psi_A\}_r^T \{\Psi_X\}_q^*|^2}{(\{\Psi_A\}_r^T \{\Psi_A\}_r^*)(\{\Psi_X\}_q^T \{\Psi_X\}_q^*)} \quad (2.16)$$

where "*" indicates the complex coniugate of the vectors.

Nowadays most of computers use a color plot, 2D or 3D, to represent the MAC magnitude.

It's important to remember that MAC is just a discrete calculation and what appears as a color contour really represents the discrete mode to mode comparison.

Here it is an example:

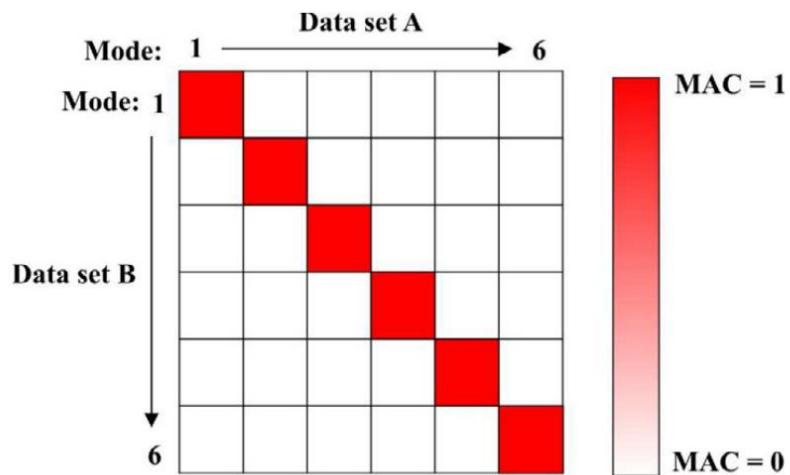


Figure 14: The MAC [6]

2.5 Forced Response

In this chapter will be analyzed the basics of *Forced Response Analysis*, which consists in the investigation of the interaction between a dynamic load with a natural frequency of the structure object of study.

Particularly a turbine disk is subjected to an aerodynamic force which has more less this behavior:

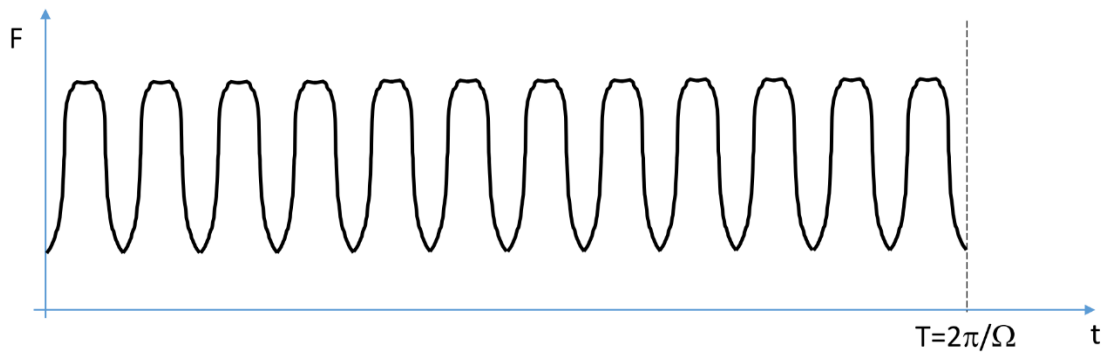


Figure 15: Aerodynamic force [7]

In this case the number of peaks of the force is equal to the number of statoric sectors in front of which the single rotor sector passes during a revolution.

If the rotational speed Ω is constant is possible to introduce the angle $\alpha = \Omega t$ and represent the force field using the Fourier series:

$$F(\alpha) = F_0 + \sum_{eo} F^{eo} \cos(eo \cdot \alpha + \delta) \quad (2.17)$$

where

$$F^{eo} = \sqrt{(F^{eo})_{\cos}^2 + (F^{eo})_{\sin}^2} \quad (2.18)$$

and

$$\tan(\delta) = -\frac{F_{sin}^{eo}}{F_{cos}^{eo}} \quad (2.19)$$

Let's consider now the generic component eo of the force, which in literature takes the name of *engine order*. Here it is an example of engine order 3, characterized by three periods inside of a round corner:

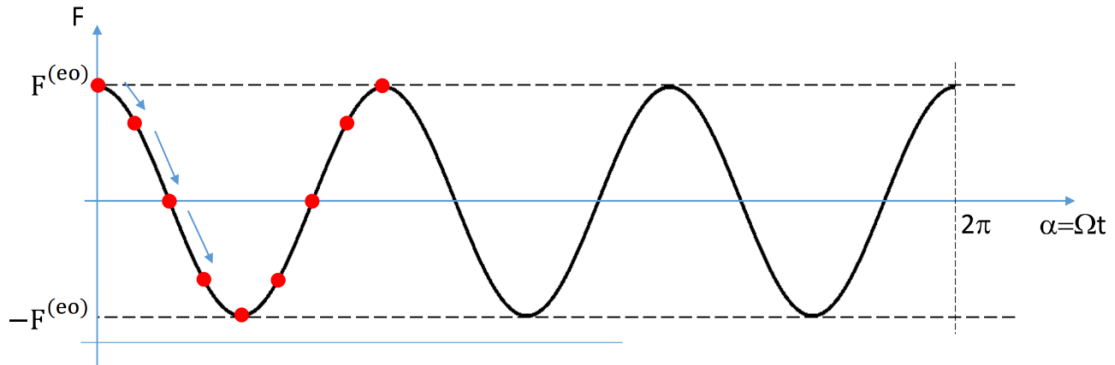


Figure 16: Example of engine order [7]

The red point indicates the position of the n sector which rotates and is stressed by a force which changes in time:

$$F^n = F^{eo} \cos(\omega \cdot t + \delta) \quad (2.19)$$

and $\omega = eo \cdot \Omega$.

Let's now consider two adjacent sectors which pass in front off the pressure field:

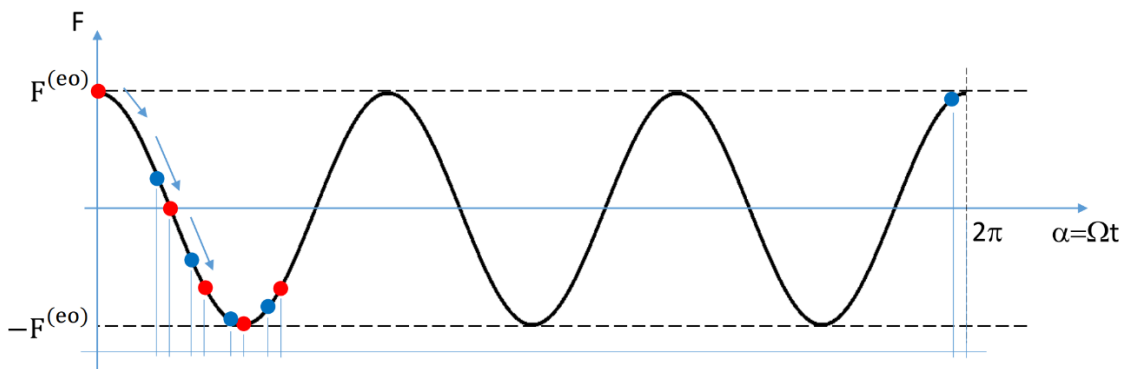


Figure 17: Two sectors [7]

In this case the red point indicates the position of the n sector and the blue point the position of the $n+1$ sector.

The time lag between them is:

$$\Delta t = \frac{2\pi}{\Omega N} \quad (2.20)$$

It's easily to demonstrate that in presence of an engine order eo the forces that act on two adjacent sectors are out of phase between them in time of an angle:

$$\psi = eo \frac{2\pi}{N} \quad (2.21)$$

The most important instrument for doing a forced response analysis is the *Campbell diagram*, proposed by Wilfred Campbell in 1924, in which on the x -axis there is the rotational speed and on the y -axis the natural frequencies of the studying structure.

Here it is an example:

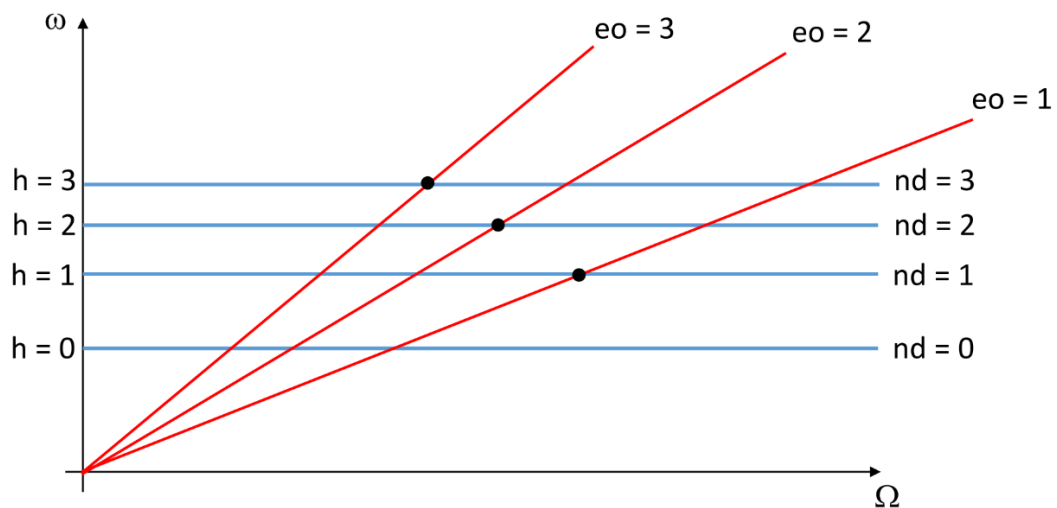


Figure 18: Campbell diagram [7]

In the upper figure it's possible to observe a theoretical diagram. This type of diagram could also be determined with experimental measurements, using a group of strain gauges.

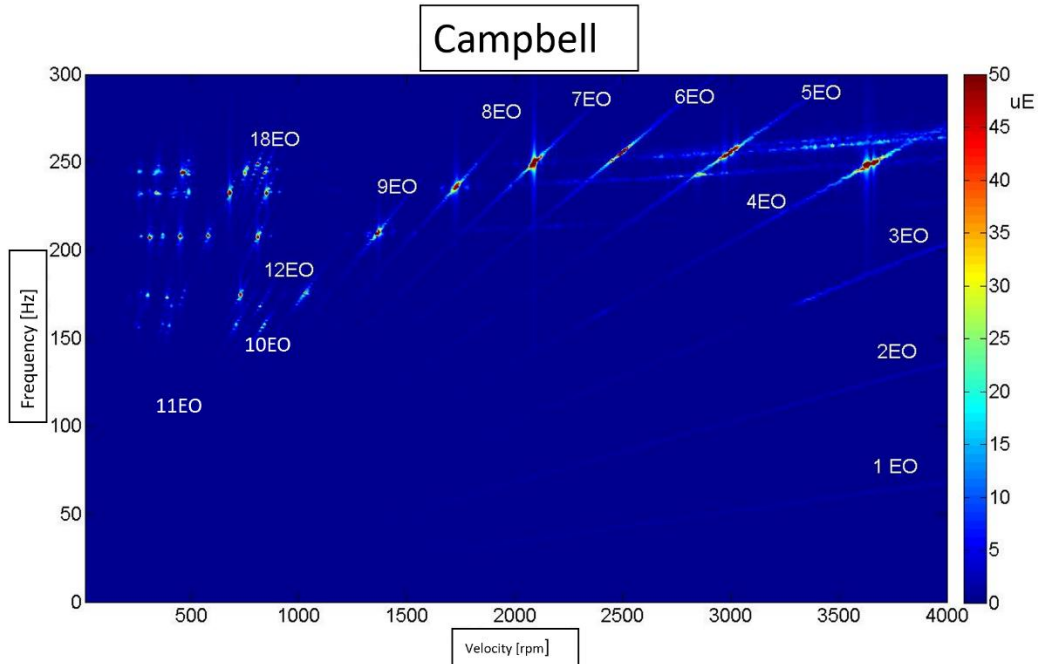


Figure 19: Experimental Campbell diagram [8]

In the picture above it's possible to see that not all the crossing point on the diagram could cause *resonance*. In fact it's easy to demonstrate that, because the forcing could have an engine order greater than $N-I$, to have resonance it's necessary to verify the following relation:

$$eo' = eo - kN = h \quad (2.22)$$

where eo is the engine order, N is the number of sectors of the disk, h is the harmonic index and k is the molteplicity.

Otherwise, if N is odd:

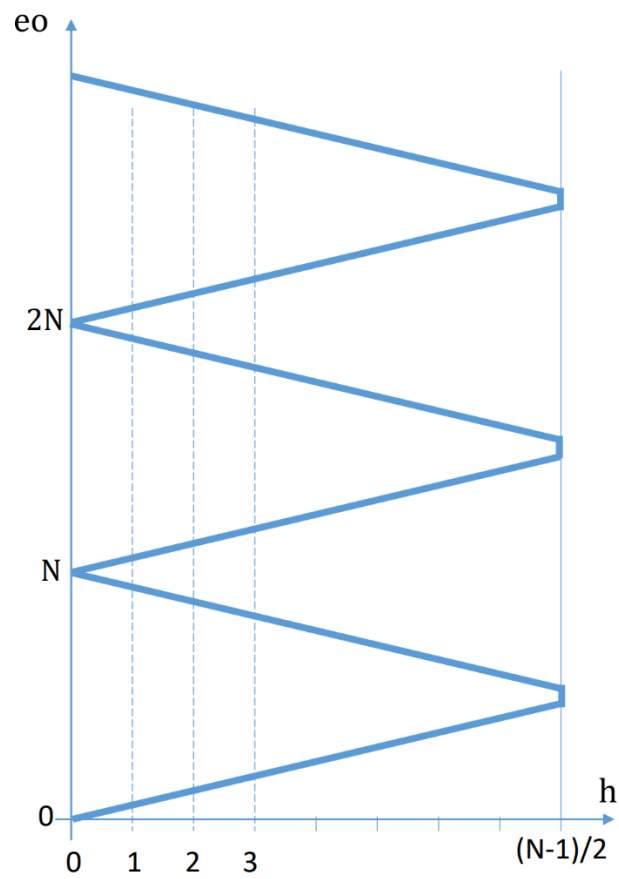


Figure 21: Zig – Zag diagram: N odd [7]

Chapter 3

Aeroelasticity in turbomachinery

In this chapter will be introduce the theoretical basis of aeroelasticity, that is a part of the aerospace engineering which studies the interaction between fluid and structure.

The *Collar diagram* is probably the best instrument to resume the elements of this science.

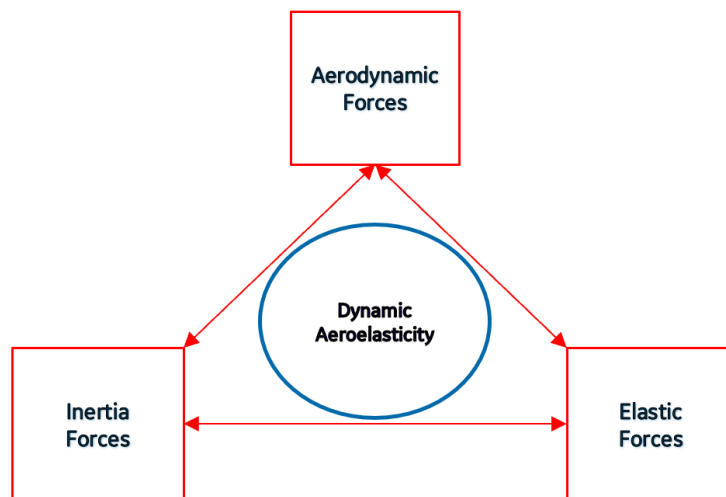


Figure 22: Collar diagram

Aeroelasticity is a very wide field of study and particularly in this chapter will be studied the *dynamic aeroelasticity*, which is the study of the interaction between

the fluid with one or more modes of the structure. This phenomenon is called *flutter* and it is a self-sustained aeromechanics phenomenon, which could be seen on the Campbell diagram as an asynchronous vibration.

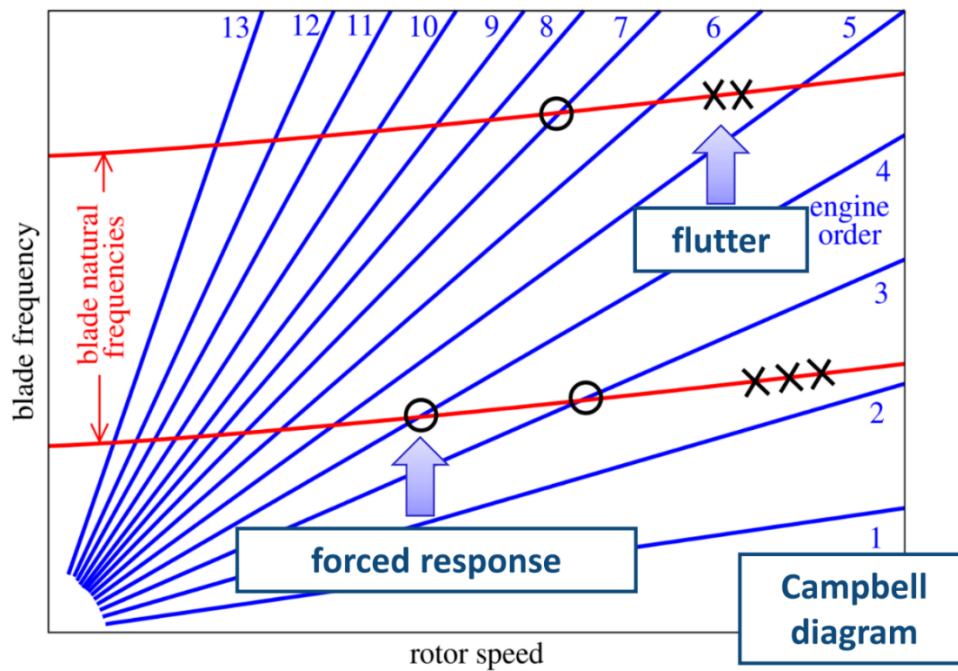


Figure 23: Flutter vibrations on Campbell diagram [4]

This type of phenomena started to be object of study especially after the collapse of the Tacoma Narrows bridge in 1940. In that situation the wind put in flutter the torsional mode of the bridge, causing the destruction of it.



Figure 24: Tacoma Narrows bridge [22]

In that period Theodore Theodorsen proposed a first aerodynamic method to study these phenomena, in which aerodynamics parameters (Lift and Bending moment) were studied in function of velocity. If it exceeds a specific critical value flutter may occur.

After this first approach in the following years were developed some methods based on panel's theory, in which the scientists for the first time tried to couple the FEM results with the aerodynamic loads. These methods are VLM (Vortex Lattice Method) and DLM (Doublet Lattice Method). They are quite accurate, but the drawback of them is that they are based on the *potential fluid*, so in some situations could present non acceptable results.

Today the state of the art of aeroelastic analysis consists in a 3D detailed CFD analysis associated to a structural modal analysis, in the way to perfectly study the fluid structure interaction.

After this introduction to dynamic aeroelastic phenomena, in the next paragraph will be analyzed the problem of the fluid – structure interaction especially in turbomachinery.

3.1 Aircraft engine aeroelasticity

In this section is studied the phenomenon of flutter in jet engines.

The most critical part of them under the aeroelastic point of view are the slender blades with a high aspect ratio: fan blades and LPT blades. These components, which are very sensible to vibrations, could go on flutter if the fluid in some situation supplies too much aerodynamic work on them.

Flutter could be a very dangerous phenomenon, because if it appears even just in a blade channel the it could easily propagate to other channels and destroys the entire row.

Here it is an example:



Figure 25: Flutter damage in a steam turbine [5]

Let's now have a quick look to the procedure to perform a 3D flutter calculation.

As anticipated before, first of all it's necessary to perform a CFD analysis to determinate all the aerodynamics loads that acts on the turbine stage.

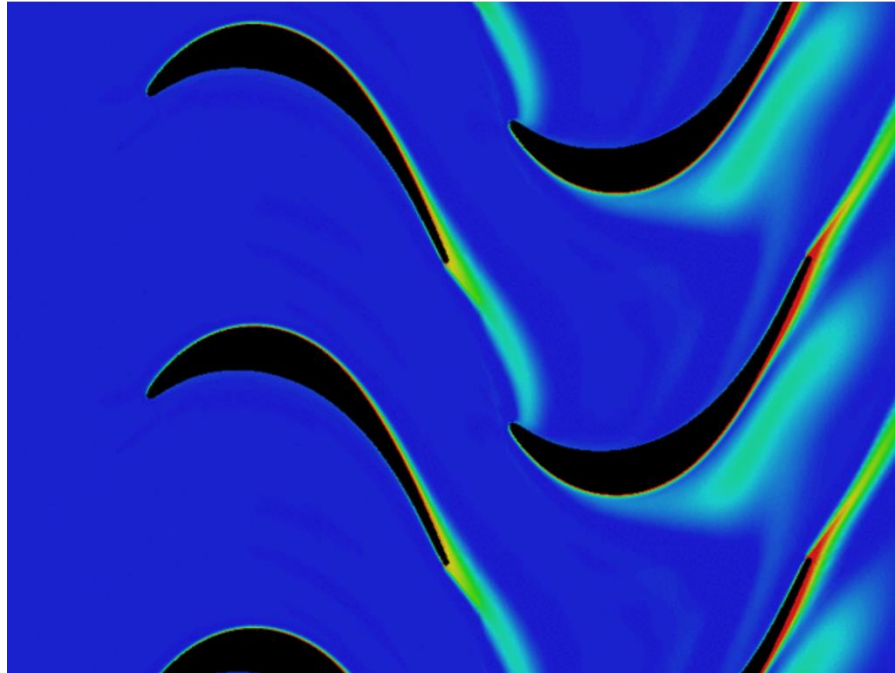


Figure 26: LPT CFD analysis [4]

In the upper picture it's possible to observe an example of a CFD field on an LPT stage. For the turbulence it's used a RANS model.

Subsequently it's necessary to perform a modal analysis on the blade model.

This is an example of the results of a modal analysis performed on a turbine blade:

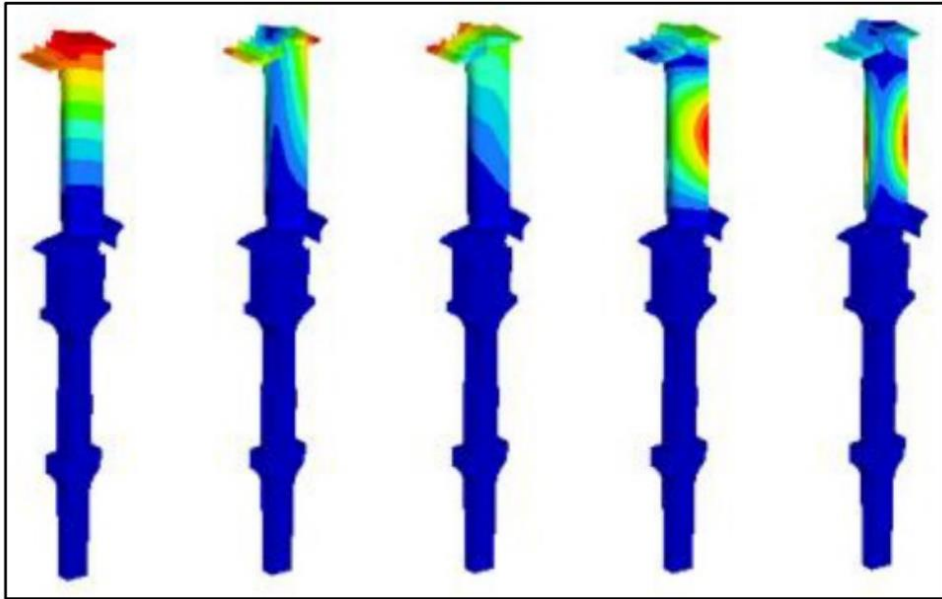


Figure 27: Modal analysis [4]

The modes that are most dangerous for the flutter response are the blade mode in which the displacement is not located in a specific zone but it involves the entire blade structure. Typically they are the 1-Flap, 1-Edge – Wise and 1-Twist.

Now the next step consists to put all the result which comes from the previously analysis in a dedicated tool which calculates, nodal diameter after nodal diameter, if the blade structure is stable or not for flutter response.

The best way to do that is to use a *coupled* approach, in which the CFD unsteady analysis and the structural dynamic analysis advance simultaneously in time. The coupled simulation starts with a random vibration and system displacement are monitored. With this approach is possible to observe the influence of the structure vibration on the fluid and the fluid vibration on the structure.

If the displacement decreases there isn't flutter, if the displacement is constant we are in a limit cycle flutter condition and last if the displacement increases we are in a flutter situation.

The picture below is helpful to understand this concept.

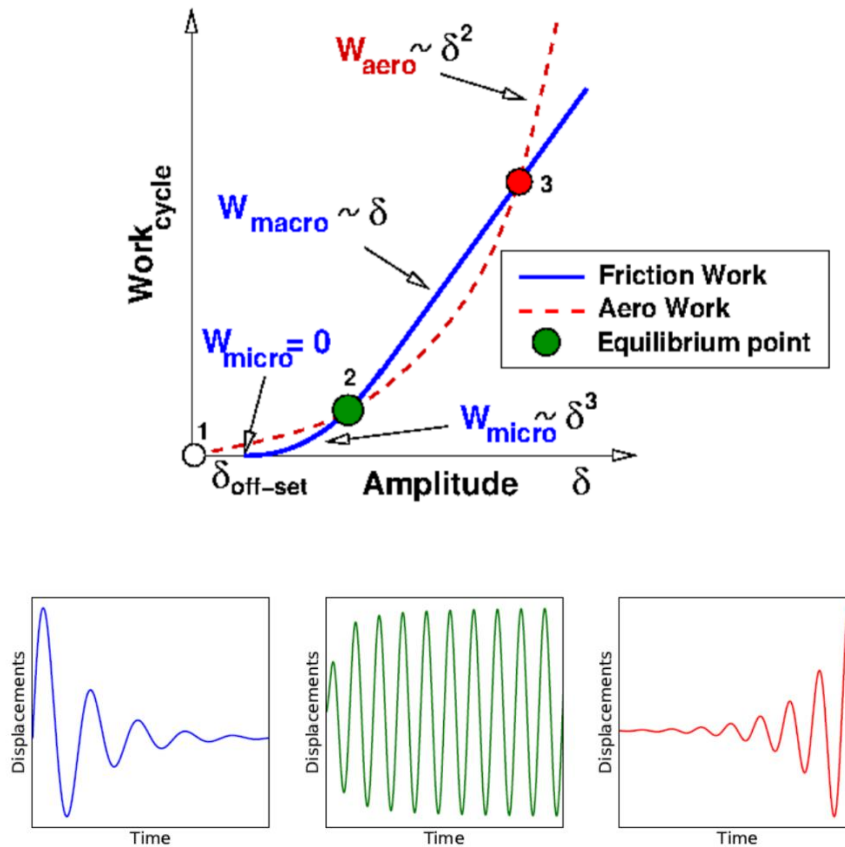


Figure 28: Coupled flutter [4]

This type of approach is very precise but it is very expensive under the computational point of view. So today in the industry panorama is preferred the *uncoupled method*, which is anyway enough accurate but above all less computational expensive.

The uncoupled approach, which is at the basis of this thesis work, will be detailed explained in the next chapter.

3.2 Flutter stability

Now it's time to define a parameter with which it's possible to understand the flutter stability. This parameter is typically the *reduced velocity*:

$$V_{red} = \frac{V}{\omega b} \quad (3.1)$$

where V is the flows velocity, ω is the blade vibratory frequency and b is the semi-chord of the profile. The reduced velocity is typically included between 1 and 5.

Decreasing this parameter is stabilizing.

In some cases it's also used the reciprocal of reduced velocity, which is called *reduced oscillatory frequency*:

$$k = \frac{\omega b}{V} \quad (3.2)$$

In this case increasing k is stabilizing.

Let's analyze now the effect of the gas density on flutter level of stability: it has a double effect. If aerodamping is positive, increasing the gas density is stabilizing. Otherwise, if aerodamping is negative, increasing the gas density is destabilizing.

The definition and the role of the aerodamping will be much clear in the next chapter.

3.2 Classification of flutter

In this section is proposed a classification of all flutter phenomena that could appear in turbomachinery.

Typically they are divided in:

- **Classical flutter:** it appears without any separations and it is caused by the phase lag between blade vibration and induced aerodynamic forces. In the next chapter will be proposed a detailed analysis of this type of flutter.
- **Coalescence flutter:** it appears when two natural frequencies are about to merge.
- **Stall flutter:** it arises near stall conditions.
- **Dynamic stall flutter:** in which the bladerow is stalled only during a part of the vibration cycle.
- **Choke flutter:** it appears near choking conditions.
- **Supersonic unstalled flutter:** a type of classical flutter that arises when the flow is supersonic.

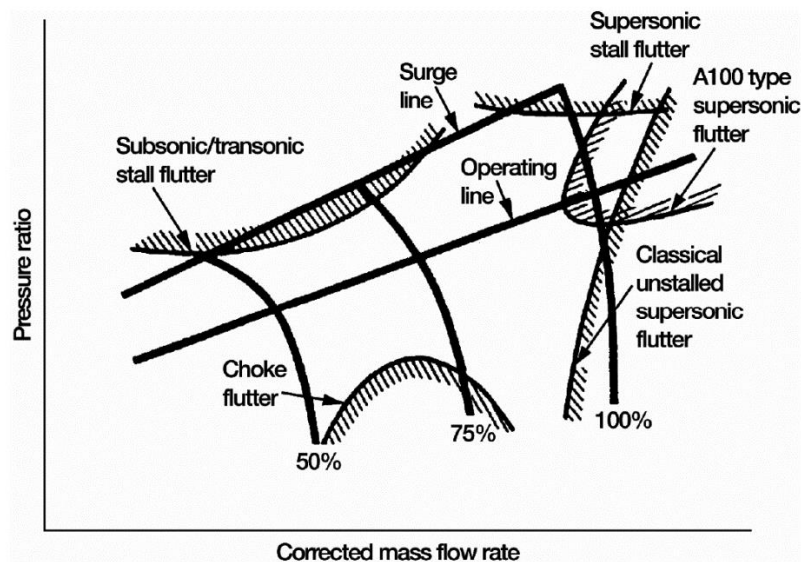


Figure 29: Classification of flutter [4]

Chapter 4

3D Flutter Analysis

This chapter is dedicated to the numerical 3D flutter analysis. In particular the first two chapters are dedicated to a detailed mathematical analysis of the numerical methods, while in the last three chapters are proposed the results of the test campaign.

4.1 The ARIAS project

As written in the abstract, ARIAS (Advanced Research Into Aeromechanical Solutions) is an European project realized to study the forced response and the level of flutter stability in turbomachinery. Inside this project a lot of different components are object of study: vanes, turbines, compressors ecc.

A lot of different entities are partners of ARIAS: factories, universities, research poles ecc.



Figure 30: ARIAS partners [24]

Our goal is to analyze the level of flutter stability of LPT blades, so our focus is referred to ARIAS 144, a cold flow test rig located at CTA in Bilbao which was built specifically for studying aeroelastic phenomena.

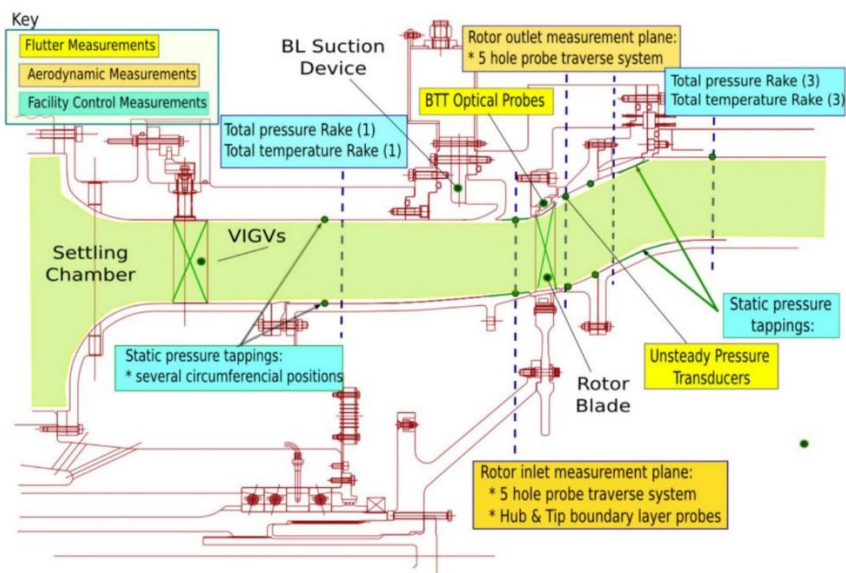


Figure 31: CTA rig [4]

Let's now have a look to the rotor bladed disk: the number of blades initially was 146 but the was reduced to 144. This because 144 is a multiple of 2 and 4, so in this way is possible also to study also pockets of 2 blades and 4 blades. This fact will be clearer in the *Conclusions* chapter of this thesis work.

In the next picture it's possible to admire the bladed disk.

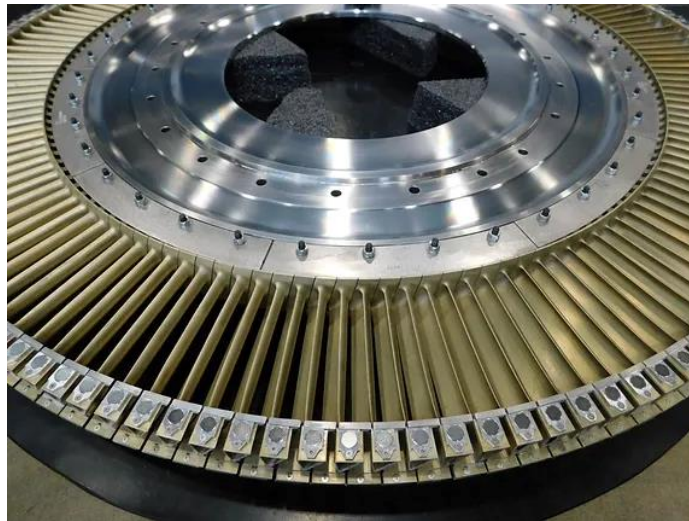


Figure 32: ARIAS cold flow bladed disk [24]

With this bladed disk it's possible to study a lot of different blade configuration, using under platform dampers, balancing masses and mistuning masses.

Next are proposed some configurations usable:

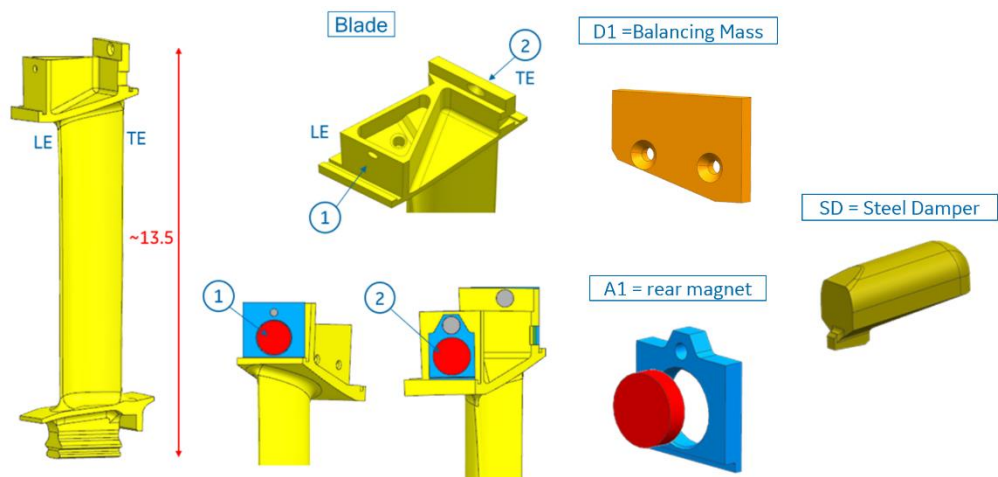


Figure 33: Some configurations [24]

After this first introduction to the cold flow bladed disk, for our numerical tests it's necessary to prepare a FEM model of them. For meshing the model was used Altair Hypermesh and then was imported in ANSYS Mechanical APDL 19.2.

The bladed disk model was realized using 3D tetra elements.

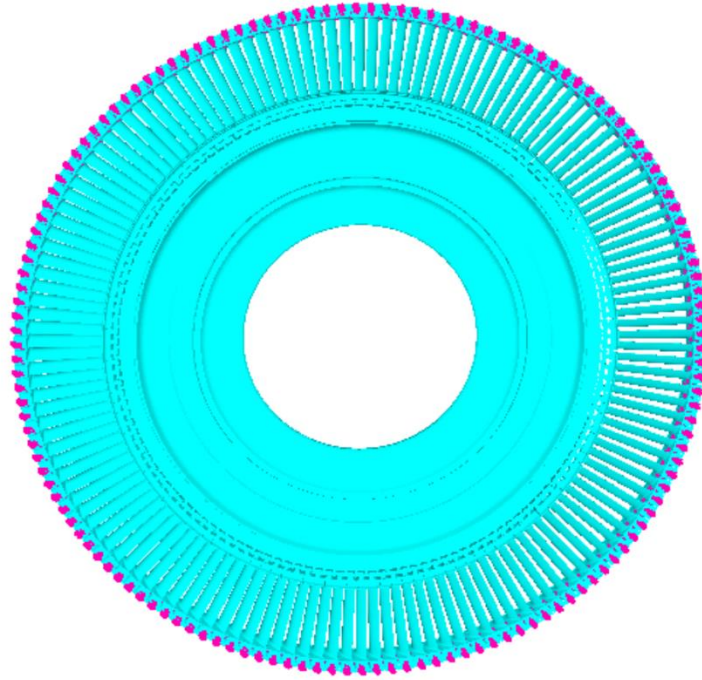


Figure 34: FEM model of the disk

Let's now have a look to the FEM model of the blade.

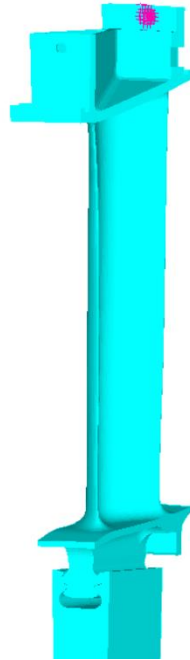


Figure 35: FEM model of the blade

So now the model of the structure is ready. In the next section will be present the results of the analysis made on this model which are at the base for performing in a second time the 3D flutter analysis.

4.2 Numerical setup

As already introduced in the previous chapters, the first step needed to perform a flutter analysis is to do a modal analysis of the structure object of study.

For our case, the bladed disk as a reference speed of 2767 rpm. So are chosen three different operational point of work:

- **Point 1:** 103 % of reference speed → Design point
- **Point 2:** 90 % of reference speed → Intermediate point
- **Point 3:** 62 % of reference speed → Off design point

The modal analysis are performed in ANSYS Mechanical APDL 19.2 with the centrifugal force as *pre – stress*.

Once the results of that analysis are obtained, it's time to prepare some files necessary for the flutter analysis.

One file contains the TRIA3 element map of the blade's skin and a second file contains the coordinates of each node of skin mesh plus the coordinates of the control nodes, which are two special nodes on the pressure side and on the suction side of the structure.

Then it's necessary to create a group of report files, one for every nodal diameters analyzed. This type of files contains real and imaginary displacement for all nodes of the skin of the blade referred to the mode selected.

In the next pages is proposed a collection of pictures of the modal analysis performed at 103 % of reference speed.

- **Mode 1, Nodal Diameter 2**

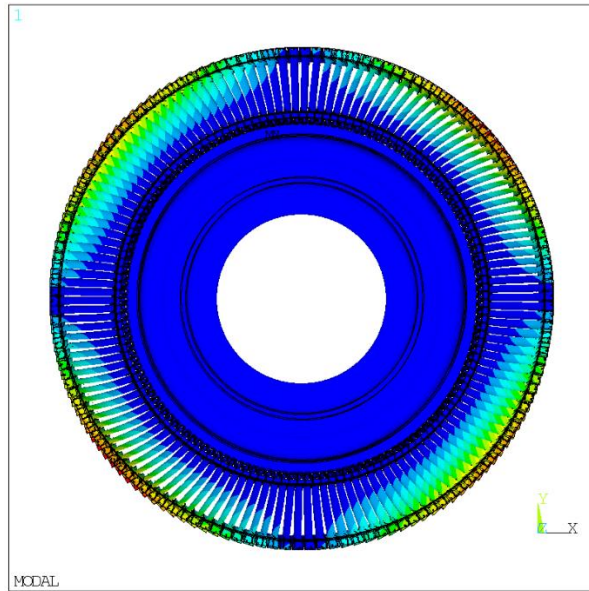


Figure 36: M 1, ND 2: Sideview

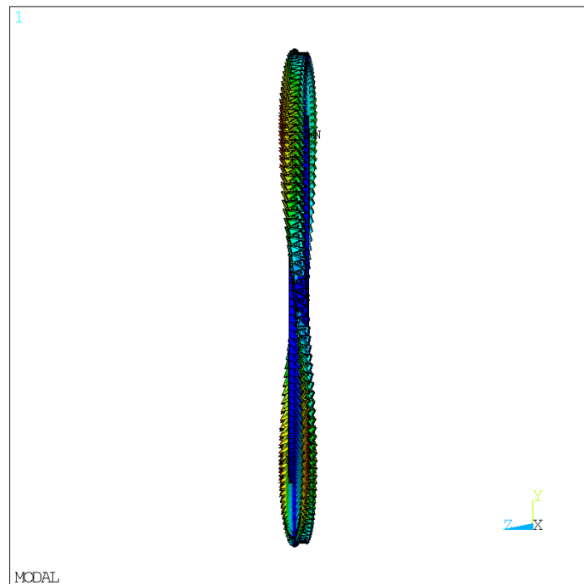


Figure 37: M 1, ND 2: Topview

- **Mode 2, Nodal Diameter 2**

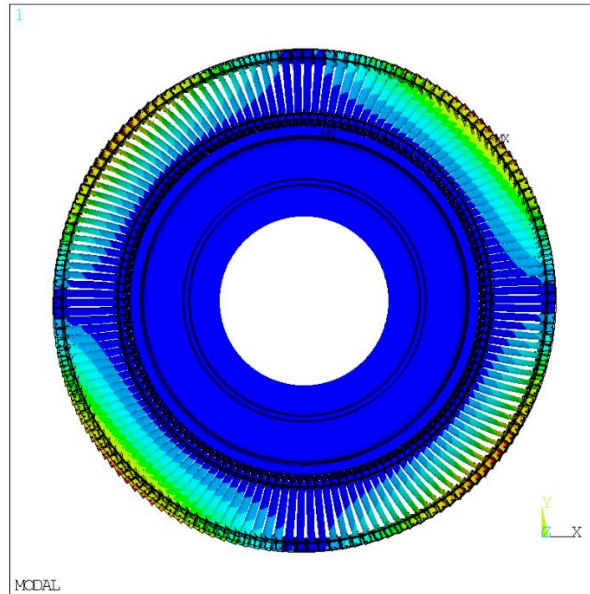


Figure 38: M 2, ND 2: Sideview

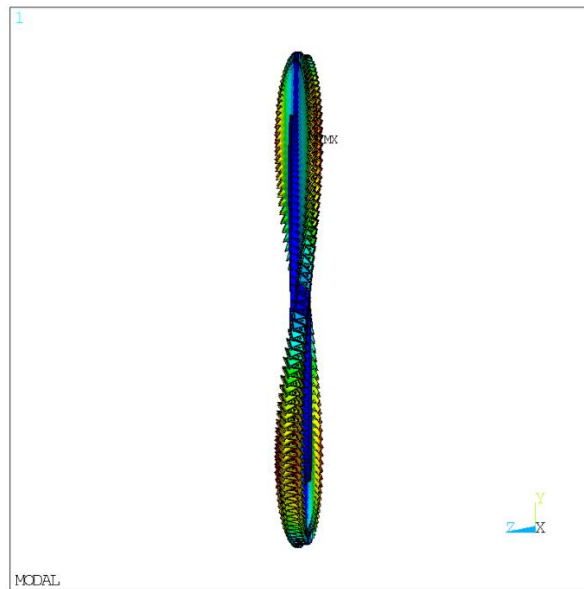


Figure 39: M 2, ND 2: Topview

- **Mode 3, Nodal Diameter 2**

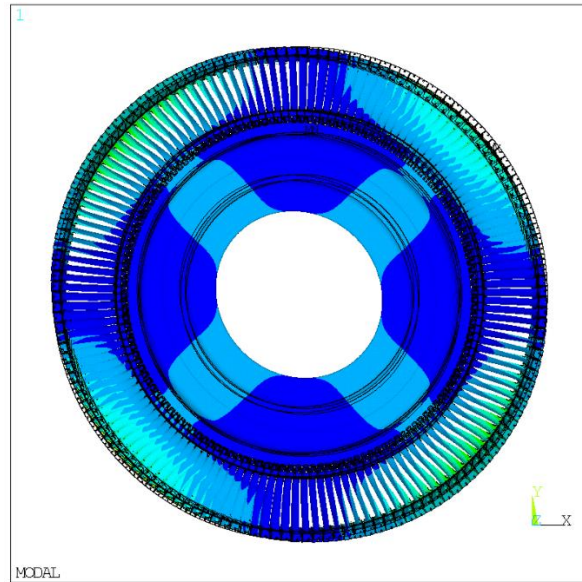


Figure 40: M 3, ND 2: Sideview

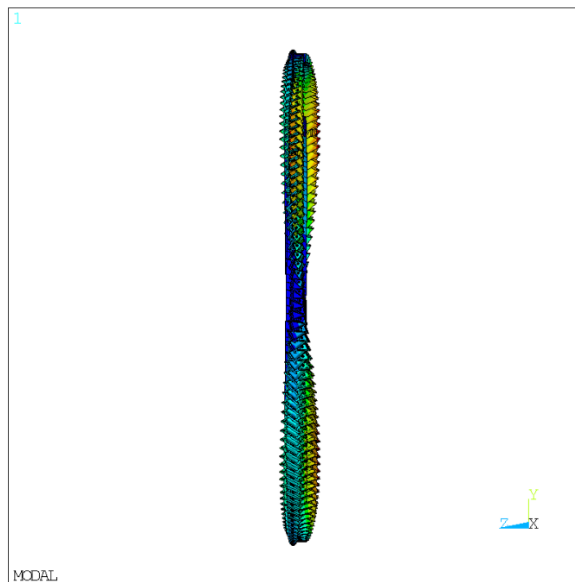


Figure 41: M 3, ND 2: Topview

- **Mode 1, Nodal Diameter 4**

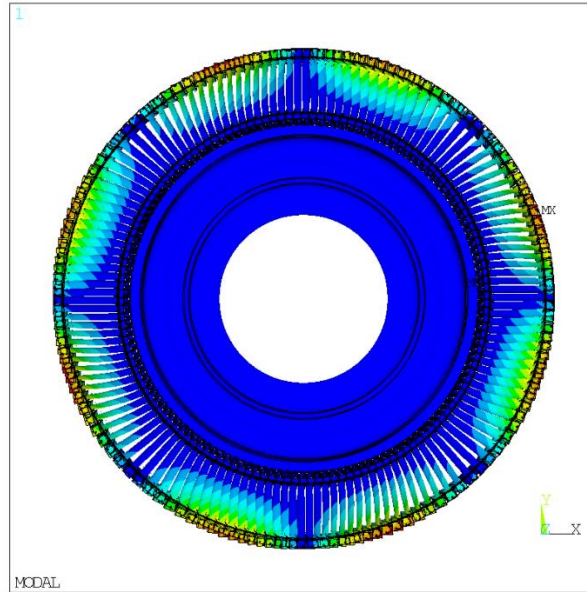


Figure 42: M1, ND 4: Sideview

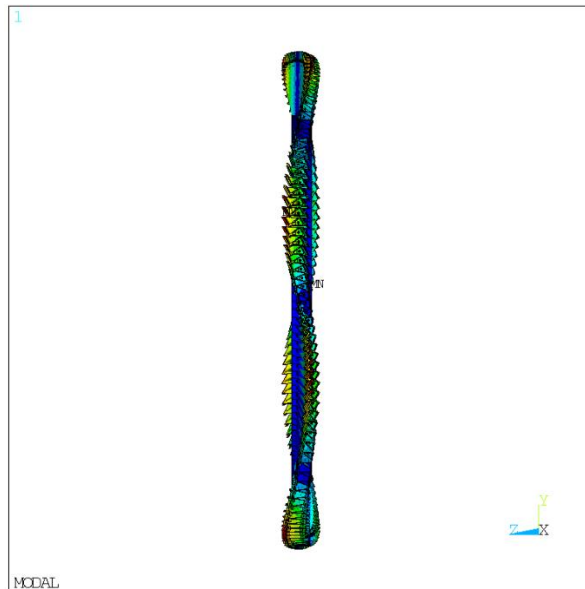


Figure 43: M 1, ND 4: Topview

- **Mode 2, Nodal Diameter 4**

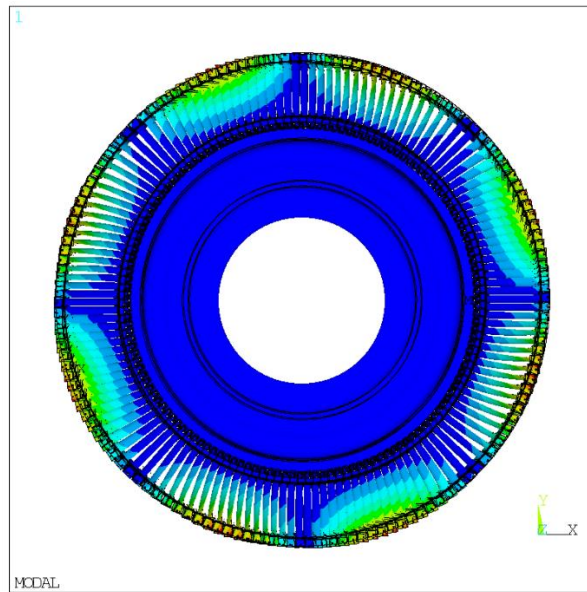


Figure 44: M 2, ND 4: Sideview

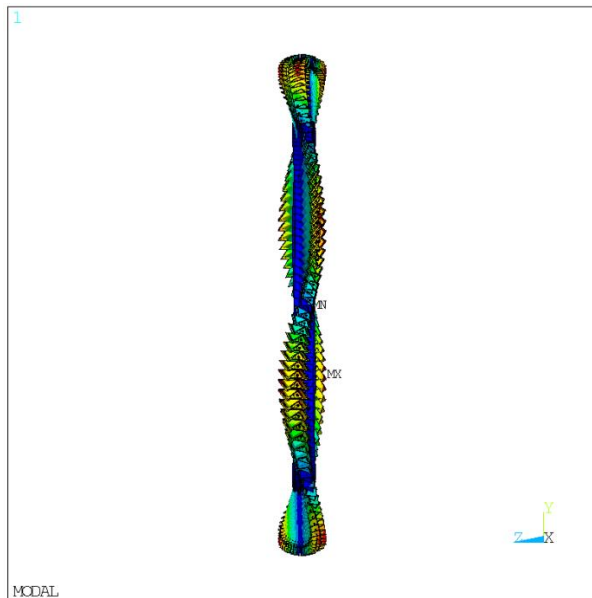


Figure 45: M 2, ND 4: Topview

- **Mode 3, Nodal Diameter 4**

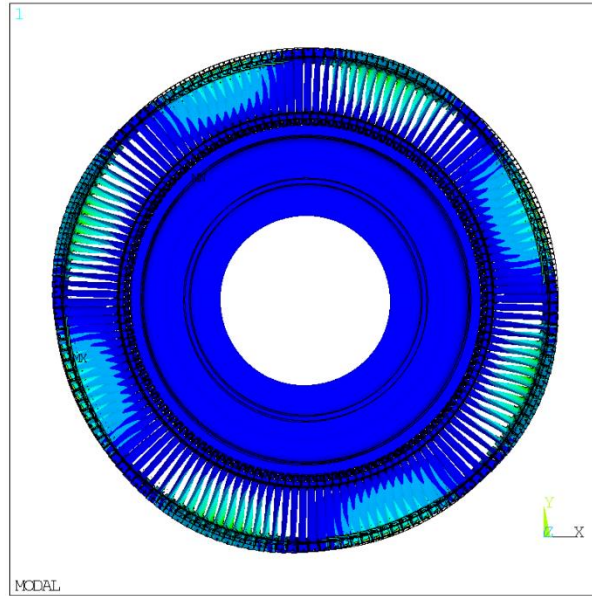


Figure 46: M 3, ND 4: Sideview

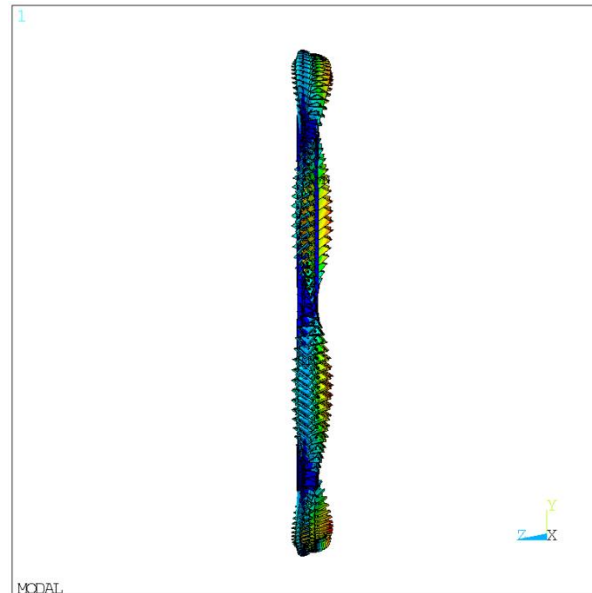


Figure 47: M 3, ND 4: Topview

- **Mode 1, Nodal Diameter 8**

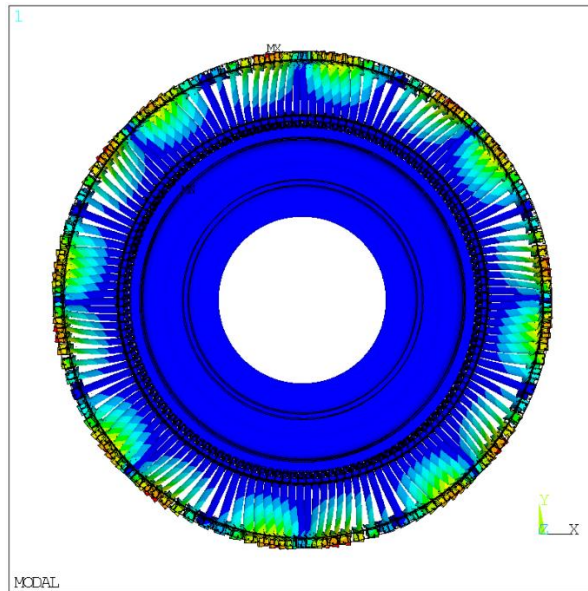


Figure 48: M 1, ND 8: Sideview

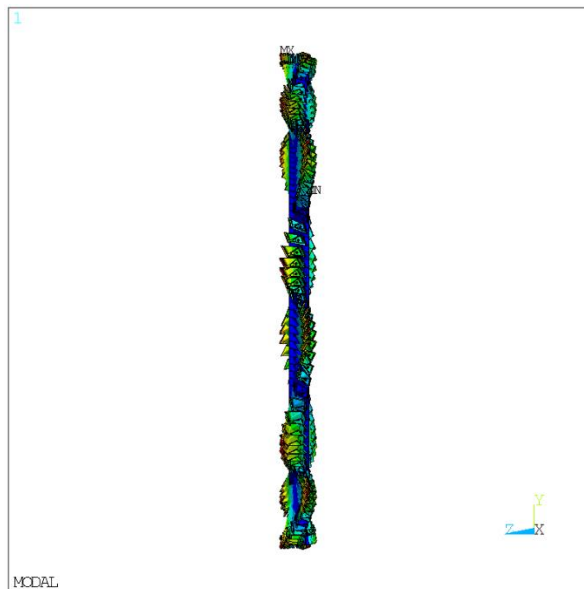


Figure 49: M 1, ND 8: Topview

- **Mode 2, Nodal Diameter 8**

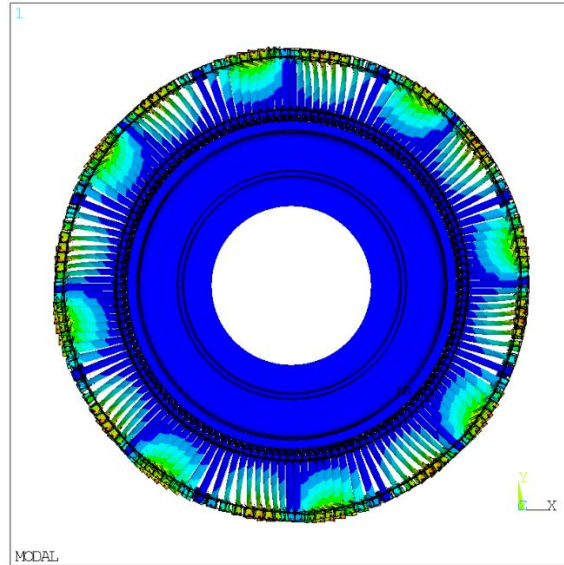


Figure 50: M 2, ND 8: Sideview

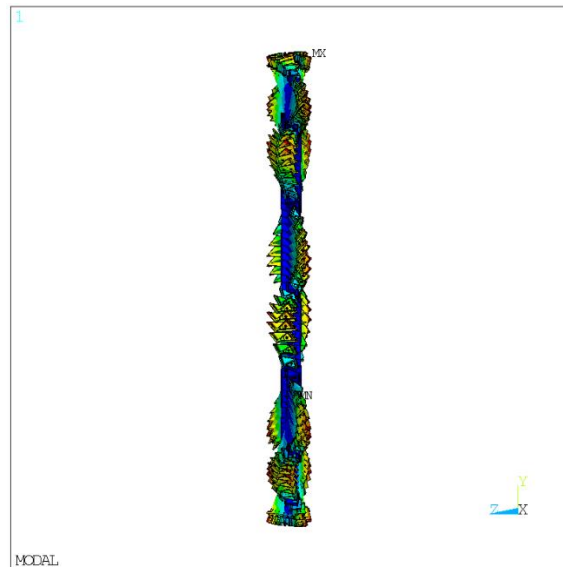


Figure 51: M 2, ND 8: Topview

- **Mode 3, Nodal Diameter 8**

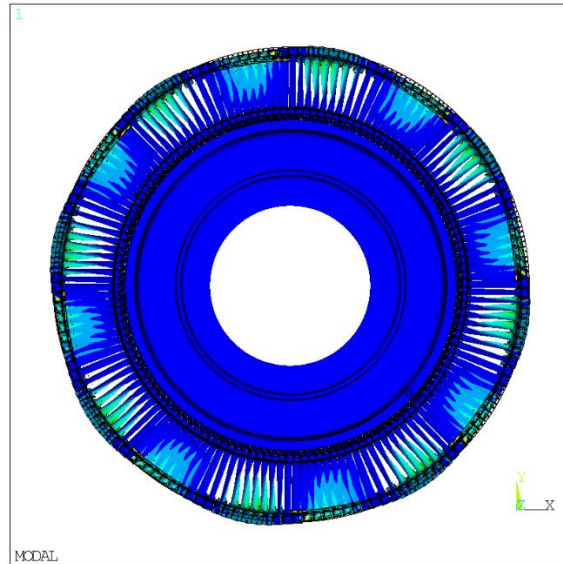


Figure 52: M 3, ND 8: Sideview

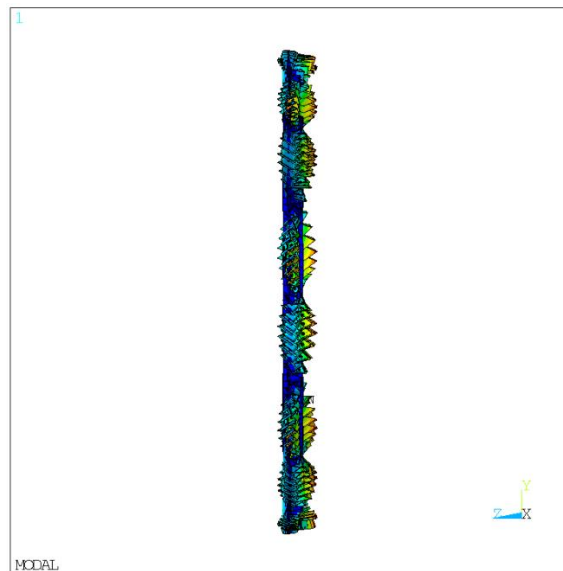


Figure 53: M 3, ND 8: Topview

So, after post processing the modal analysis, it's time to pass to the CFD calculations. For flutter analysis in fact it's necessary to perform at the beginning a CFD steady calculus in the blade's channel. The unsteadiness of the field would be treated into two different ways by the solver. This fact would be clearer in the next pages.

At the basis of our CFD calculations there is the Traf code, which is a CFD code developed by University of Florence especially for internal fluxes. It is a finite volumes code which basically works with 5 variables:

- **Inlet:** $\alpha, \beta, p_1^\circ, T_1^\circ$
- **Outlet:** p_2

Let's now define the two absolute angles:

$$\alpha = \arctan \frac{C_\theta}{C_x} \quad (4.1)$$

$$\beta = \arctan \frac{C_r}{\sqrt{C_x^2 + C_\theta^2}} \quad (4.2)$$

For the calculation of the convective fluxes it uses a TVD MUSCL scheme 2° order accurate while for the diffusive terms is adopted a centered scheme 2° order accurate. For the turbulence model, for our application is used a Baldwin – Lomax model, but there could be also used other different models, as the Wilcox $k - \omega$ or the $\gamma - Re_\theta$. For the integration in time of the Navier – Stokes equations is use a Runge – Kutta method 4° order accurate with residuals.

In our model, ARIAS 144, every blade's channel is discretized using almost 2400000 3D cells.

In the next picture is possible to visualize the CFD grid at mid – span:

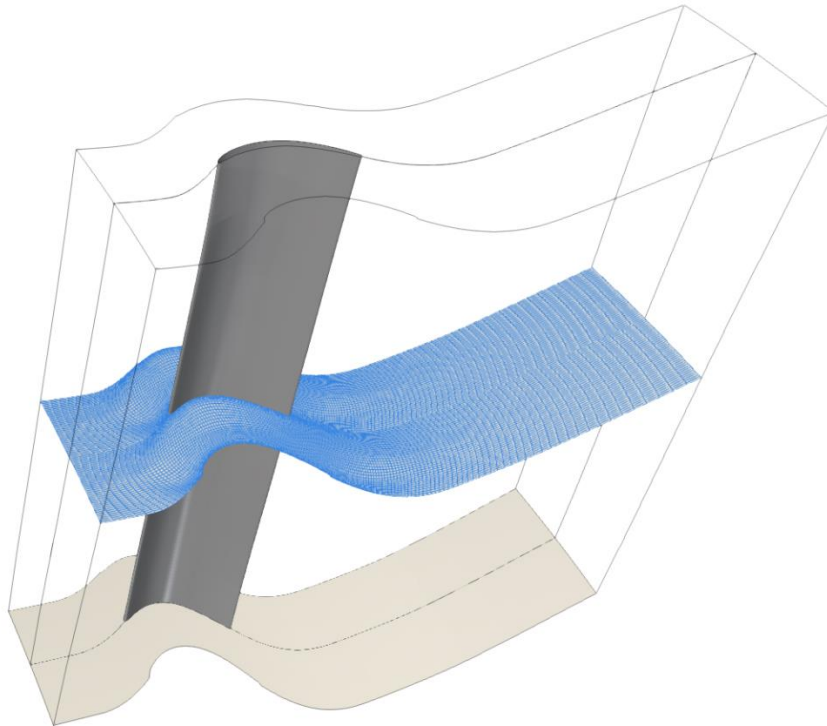


Figure 54: Mid-span mesh

So let's now have a quick look to the CFD results. In the next picture is possible to visualize the solution at 103 % of reference speed.

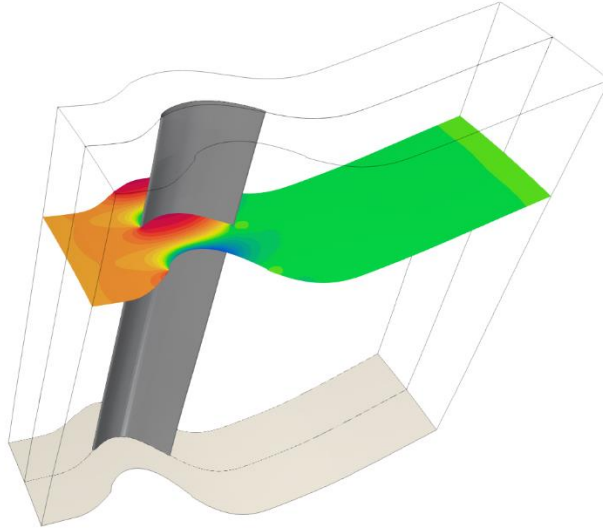


Figure 55: Pressure field

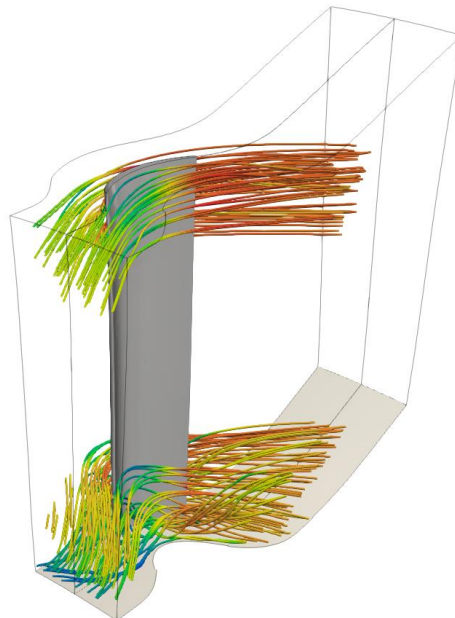


Figure 56: Streamlines

Now that both the structural and CFD analysis are computed, it's time to analyze how the flutter solvers work. They use the results of the two analysis as inputs.

As anticipated in Chapter 3, the methods used in this work are *uncoupled methods*, this because the structural and fluidic variables, which uses different grids, does not evolve together in time. In this way it's possible only to see the effect of the blade's vibration on the fluid pressure response, and not the opposite. These methods compute the value of the *aerodamping*, for every single nodal diameter. In particular it's necessary to analyze the sign of the aerodamping: if it is positive the blade is stable, while if it is negative, that means that the blade is absorbing aerodynamic work from the blade, the blade manifests flutter instability. The meaning of the aerodamping will be clearly explained mathematically in the next pages.

The two different methods are the following: a Linearized method (LARS code), which was developed first, and a Non – Linearized method (TrafNL code). At the basis of both methods there's the Traf CFD code.

The difference of the two methods consists in how they treat the unsteadiness of the field, which is directly connected with the vibration of the blade. The Linearized solver in fact sees the blade's vibration as a boundary condition, so the CFD grid is stationary and at the boundaries it senses the blade's vibration as an harmonic perturbation, while the Non – Linearized solver uses a CFD grid that directly vibrates according to the blade's vibration. So this is a time dependent method.

Let's now define the vector of the conservative variables \vec{U}' which contains information about mass, momentum, energy and turbulence quantities: while the Non – Linearized solver directly solves the time dependent part of the Navier – Stokes equations, the Linearized method makes this simplification:

$$\frac{\partial \vec{U}'}{\partial t'} = 0 \rightarrow \vec{U}' = \vec{U}_0 + \vec{U}_\delta = \vec{U}_0 + \Re[\vec{U}_\delta e^{j\omega t}] \quad (4.3)$$

where \vec{U}_0 is a mean field while \vec{U}_δ is an harmonic perturbation.

So in this way the CFD steady calculation depicted in the previous pages assumes a different role in the two solvers: in the Non – Linearized method it represents

the starting point for the evolution in time of the conservative variables, while for the Linearized method it represents the mean field around it is built the solution.

Let's now describe the role of the aerodamping. For our structure object of study, the general equation of motion could be written as:

$$m\ddot{x} + c\dot{x} + kx = F_{aero} + F_{ext} \quad (4.4)$$

In case of flutter phenomena only F_{aero} is present.

Now it's possible to compute the aerodynamic work:

$$L = \int_t^{t+T} \int (-p)\vec{N} \cdot \vec{c}_{blade} d\Sigma dt \quad (4.5)$$

where p is the pressure, \vec{c}_{blade} is the blade's chord and Σ is the blade's surface.

Finally it's possible to calculate the aerodamping as:

$$\xi = \frac{-L}{8\pi E_k} \quad (4.6)$$

where E_k is the average kinetic energy.

As already told before, it is important to analyze the sign of this value to understand the flutter stability.

In the next picture it's possible to observe the typical graphic which is the output of the flutter calculation:

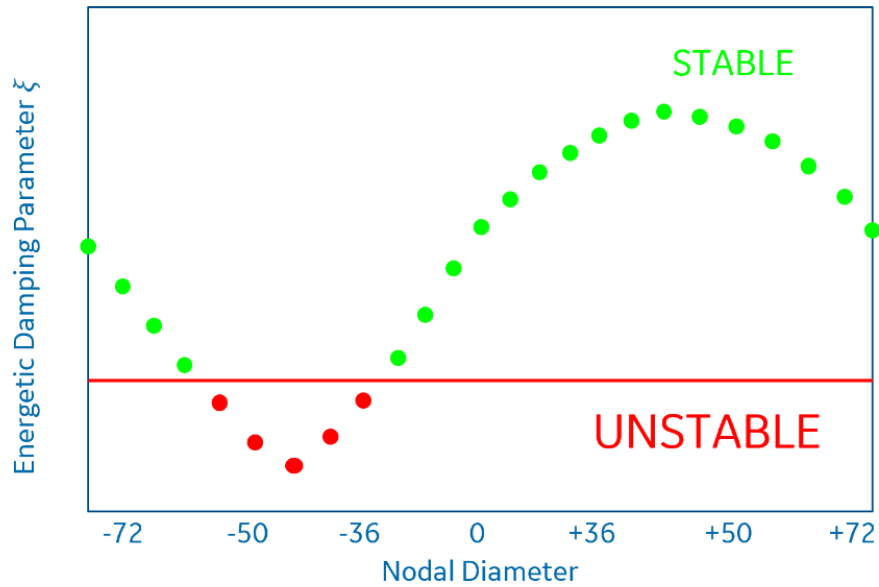


Figure 57: Flutter report

So, after this long and detailed introduction to the 3D uncoupled flutter methods, it's time to pass to the specific calculations.

4.3 Sensitivity around the operational point

In this chapter are presented the results of the numerical flutter investigation changing the engine operational point of work.

For this numerical campaign is used the Linearized solver, in the way to simulate the first approach to the problem by the engineers.

For this sensitivity is chosen the configuration of the blade A1D1: rear magnet + balancing mass.



Figure 58: Blade A1D1

For the FEM model, the rear magnet and the balancing mass are modelled as “lumped mass”.

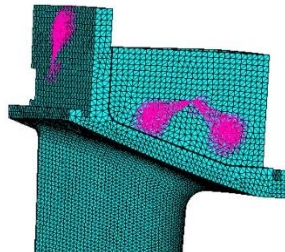


Figure 59: A1D1 FEM model

The balancing mass is used in a cold flow rig to balance the blade’s structure.

For all the sensitivity presented in this work are studied the Mode 1 and the Mode 2 because, se already told in chapter 3, they are the most dangerous for flutter stability because they could extract a lot of aerodynamic work from the fluid.

Here they are:

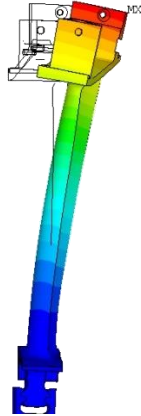


Figure 60: Mode 1

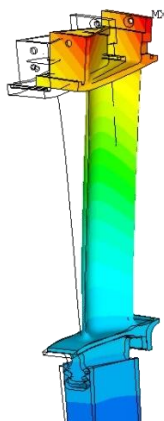


Figure 61: Mode 2

It's easy to note that the Mode 1 is the typical 1 – Flap mode, while the Mode 2 is the 1 – Edge – Wise mode. It's important to underline that this last, increasing the nodal diameter, tends to become a torsional mode. This detail will be very important in the last part of this paragraph.

For this modal analysis are chosen 11 nodal diameters, from 1 to 71, with a step of 7: 11 positive nodal diameters and 11 negative nodal diameters.

- **103 % of reference speed**

This is the On – Design point of work.

From the structural analysis is possible to create the FreND diagram:

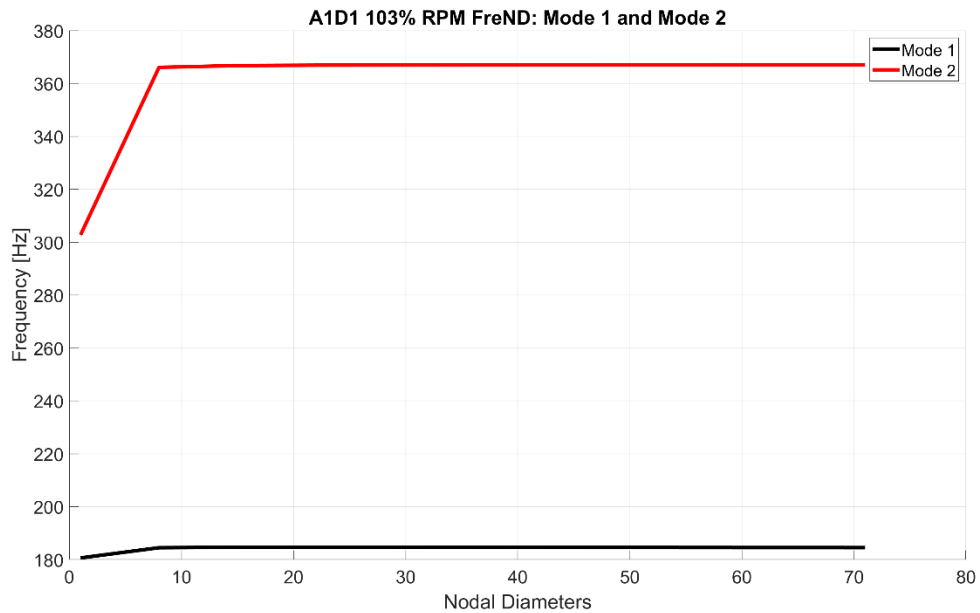


Figure 62: FreND A1D1 103 % RPM

So now it's the moment to perform the CFD steady calculation: this is done for a single blade's channel extracting the datas from a multirow CFD calculations that could come from another team in the factory or from another University.

Here they are:

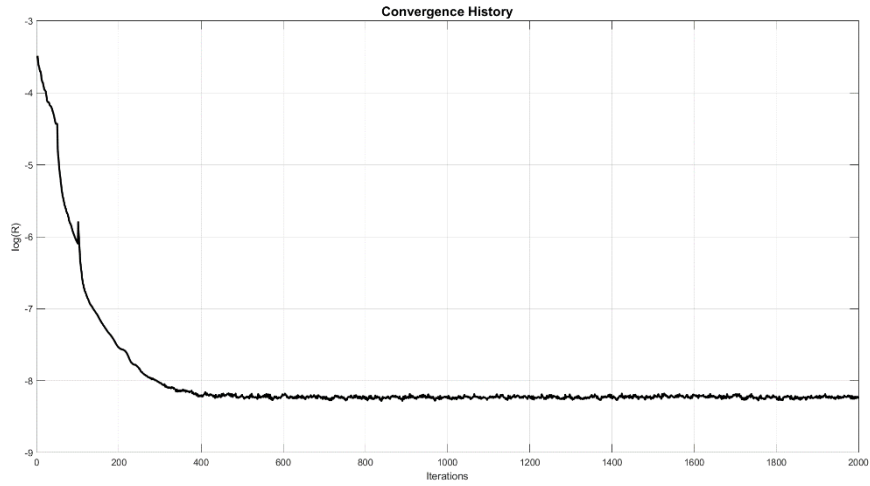


Figure 63: Convergence 103 % RPM

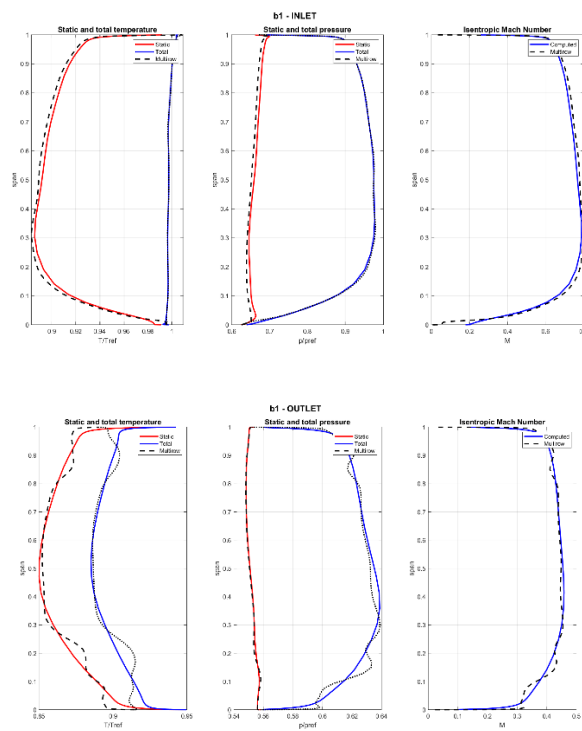


Figure 64: Inlet and Outlet 103 % RPM

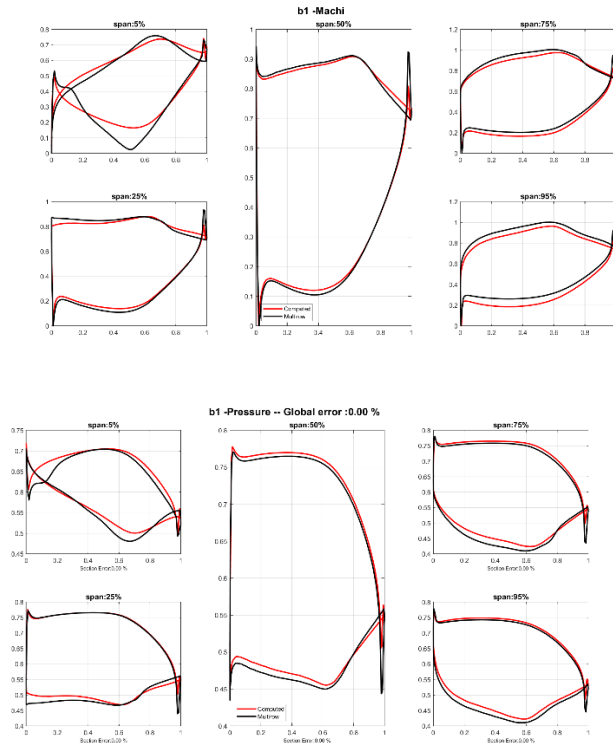


Figure 65: Mach and Pressure 103 % RPM

Now it's possible to perform the 3D flutter calculation using LARS:

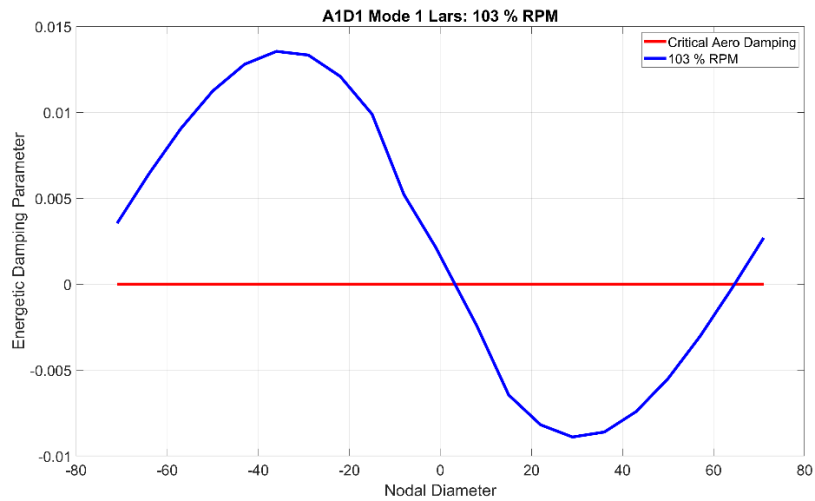


Figure 66: Aerodamping A1D1 103 % RPM: Mode 1

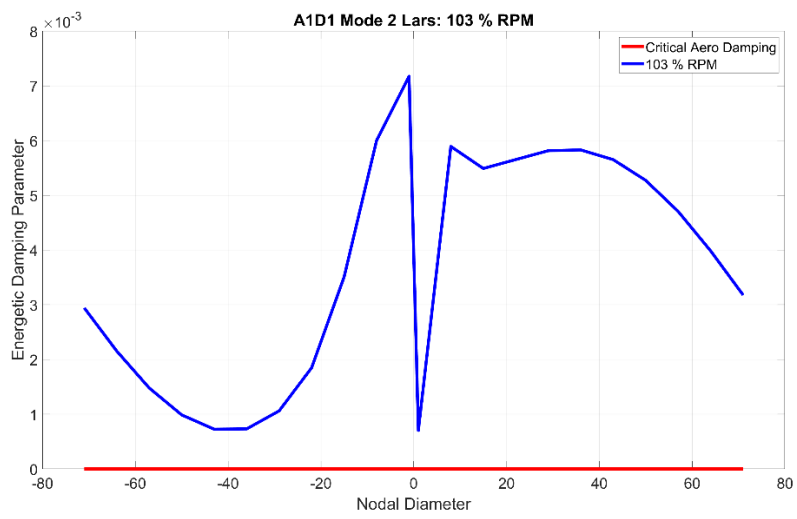


Figure 67: Aerodamping A1D1 103 % RPM: Mode 2

- **90 % of reference speed**

This is the intermediate operational point of work.

The procedure is the same, here it is the FreND diagram:

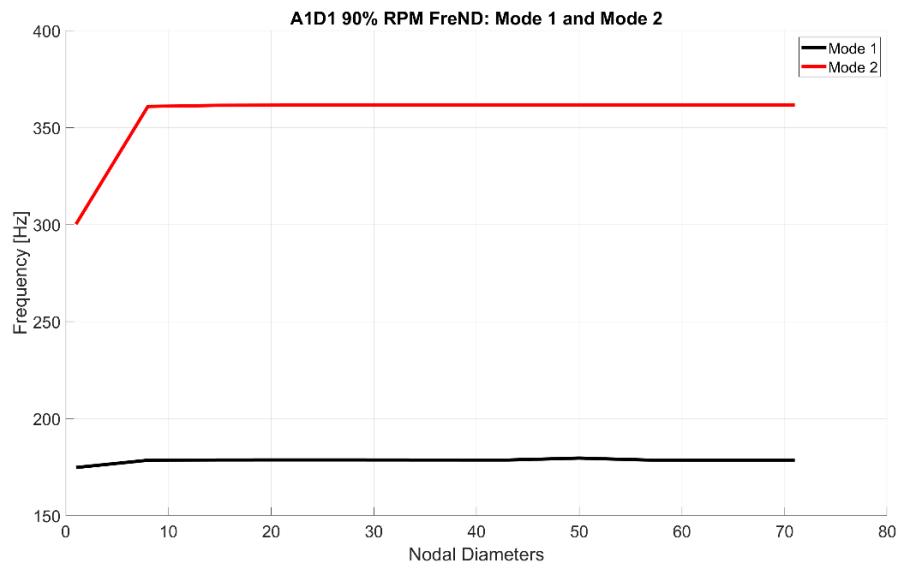


Figure 68: FreND A1D1 90 % RPM

The behavior is clear: decreasing the rotational speed, then the natural frequencies decrease.

Now let's show the results of the CFD steady calculations:

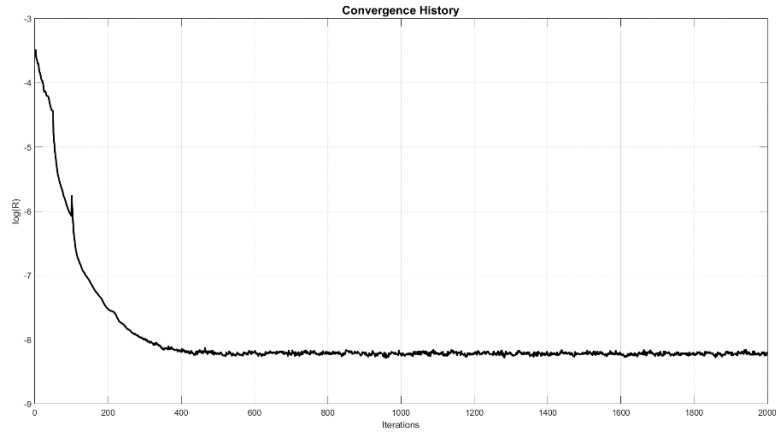


Figure 69: Convergence 90 % RPM

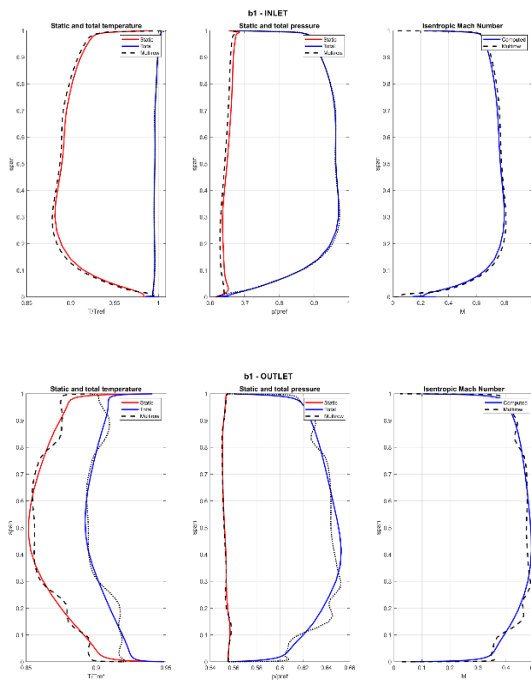


Figure 70: Inlet and Outlet 90 % RPM

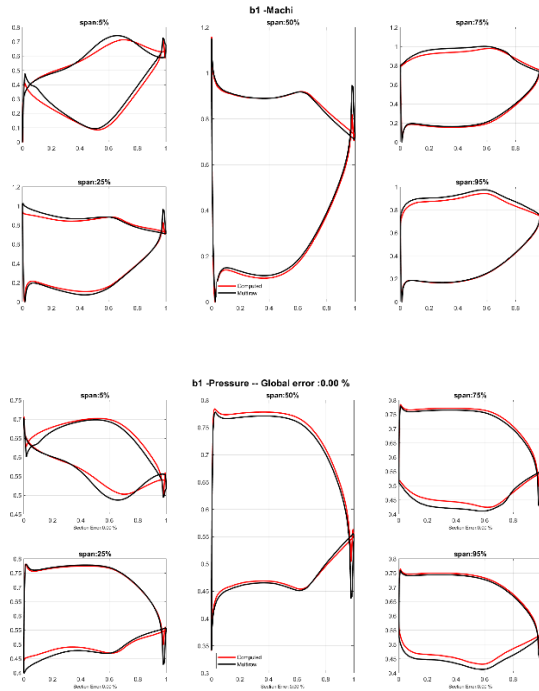


Figure 71: Mach and Pressure 90 % RPM

Now it's possible to perform the 3D flutter calculation using LARS:

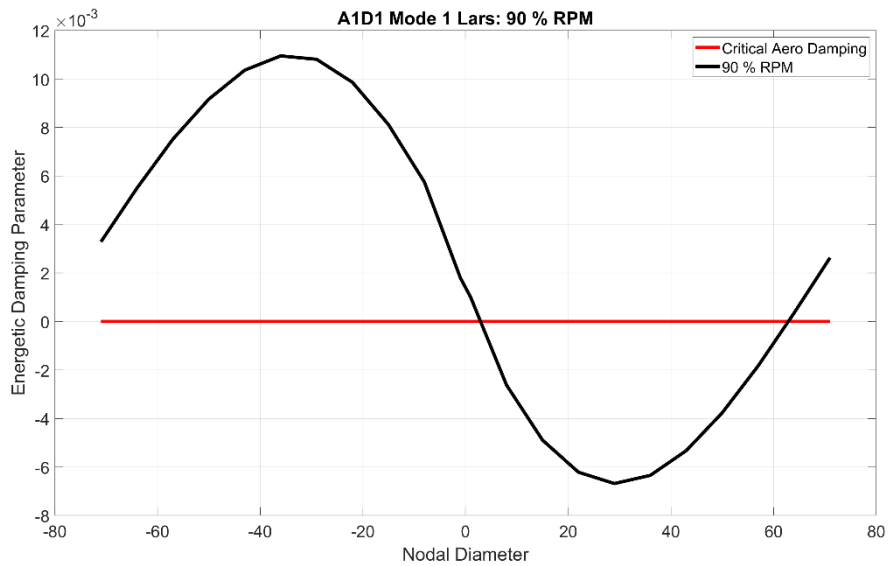


Figure 72: Aerodamping A1D1 90 % RPM: Mode 1

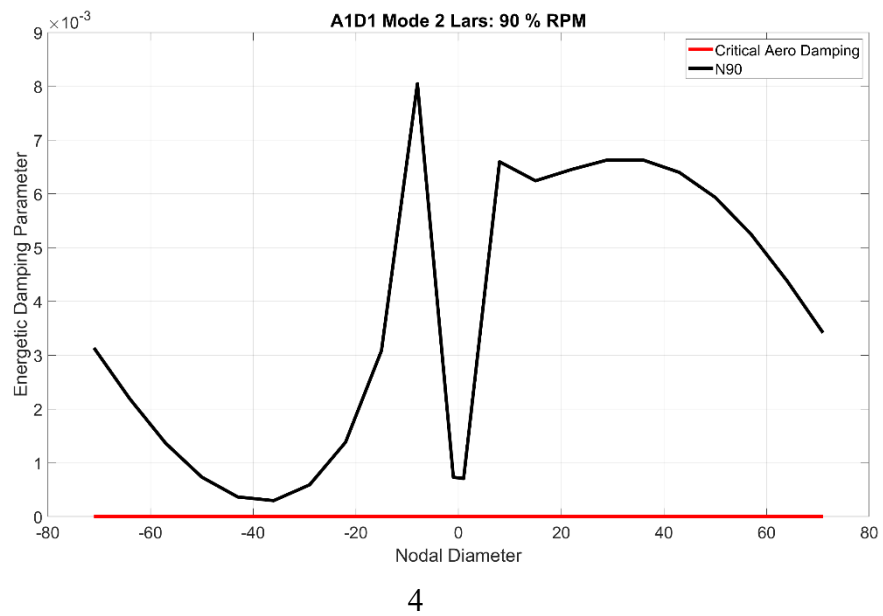


Figure 73: Aerodamping A1D1 90 % RPM: Mode 2

- **62 % of reference speed**

This is the Off – Design point of work.

Here it is the FreND diagram:

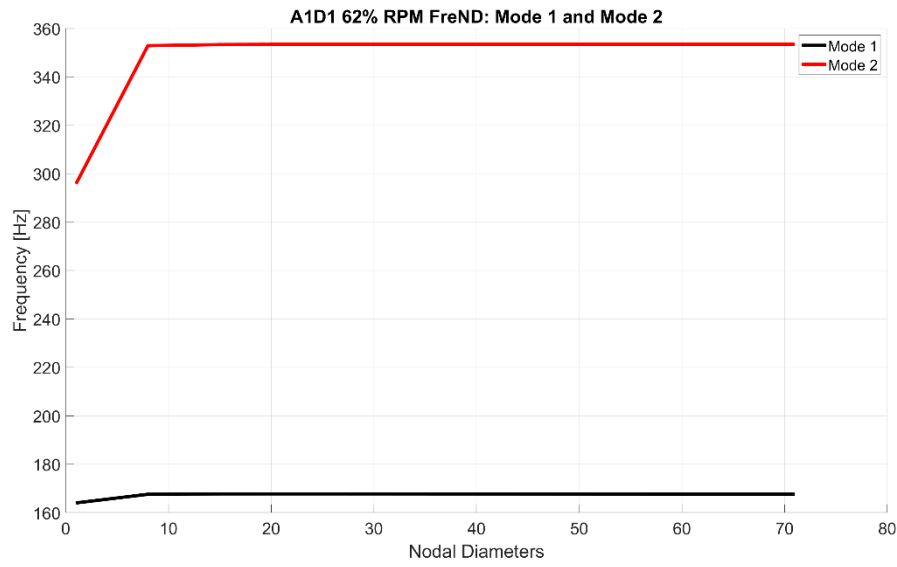


Figure 74: FreND A1D1 62 % RPM

The natural frequencies decrease again.

Now let's show the results of the CFD steady calculation:

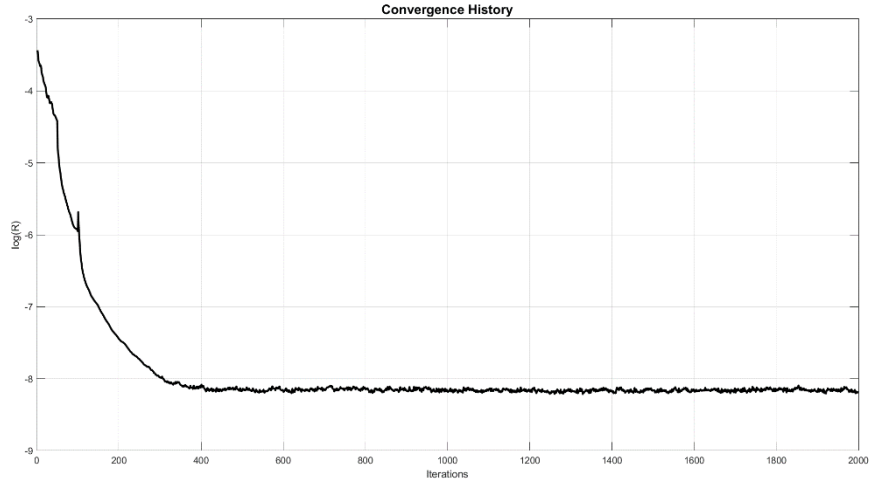


Figure 75: Convergence 62 % RPM

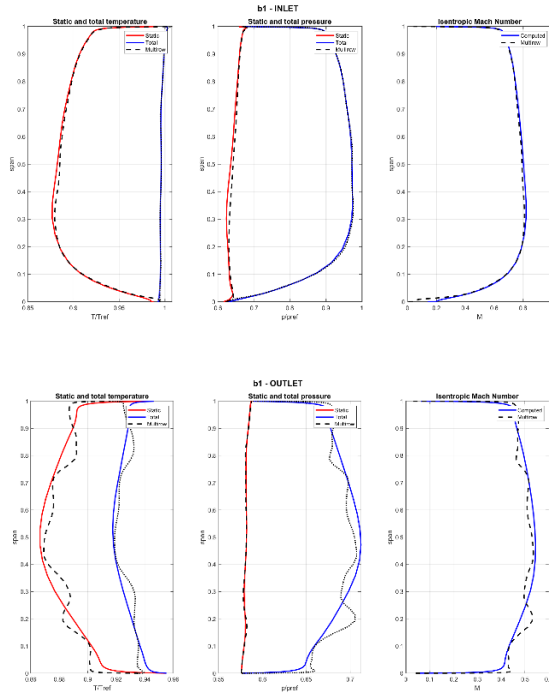


Figure 76: Inlet and Outlet 62 % RPM

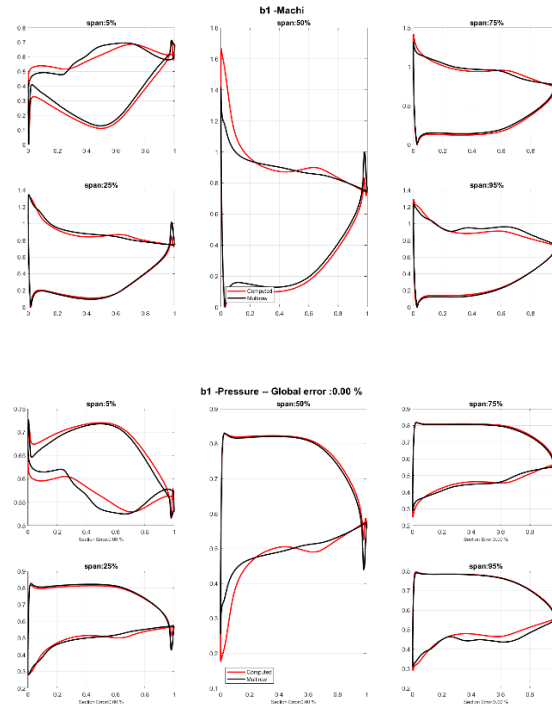


Figure 77: Mach and Pressure 62 % RPM

Now it's possible to perform the 3D flutter calculation using LARS:

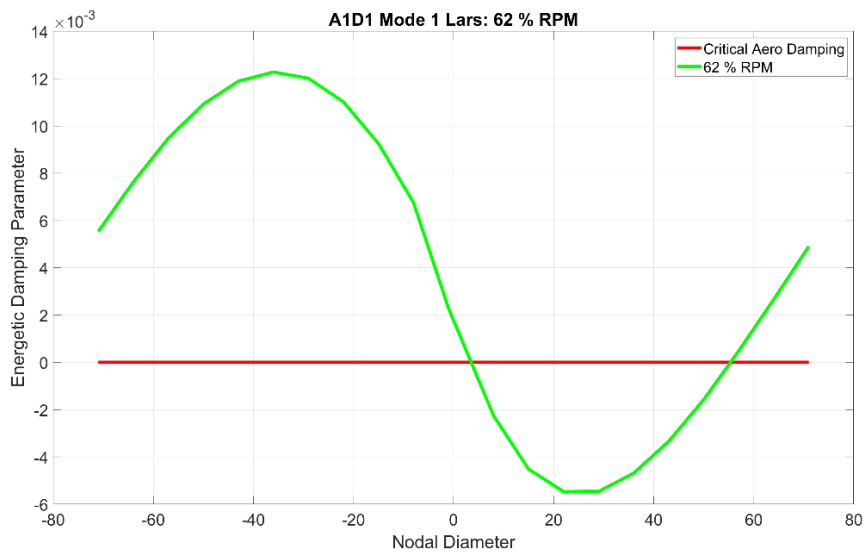


Figure 78: Aerodamping A1D1 62 % RPM: Mode 1

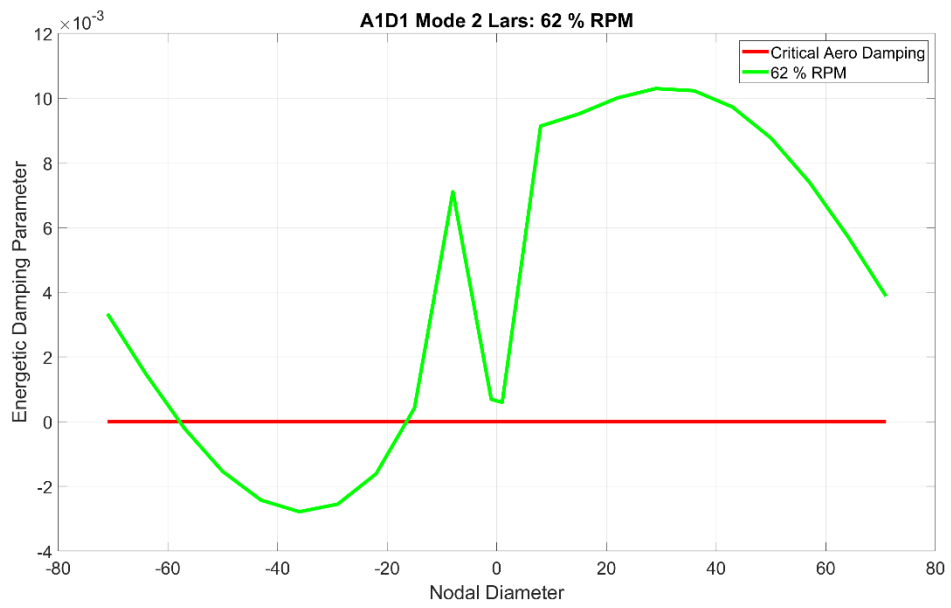


Figure 79: Aerodamping A1D1 62 % RPM: Mode 2

- **Comparison**

Now let's plot all the curves in a unique graphic, one for each mode:

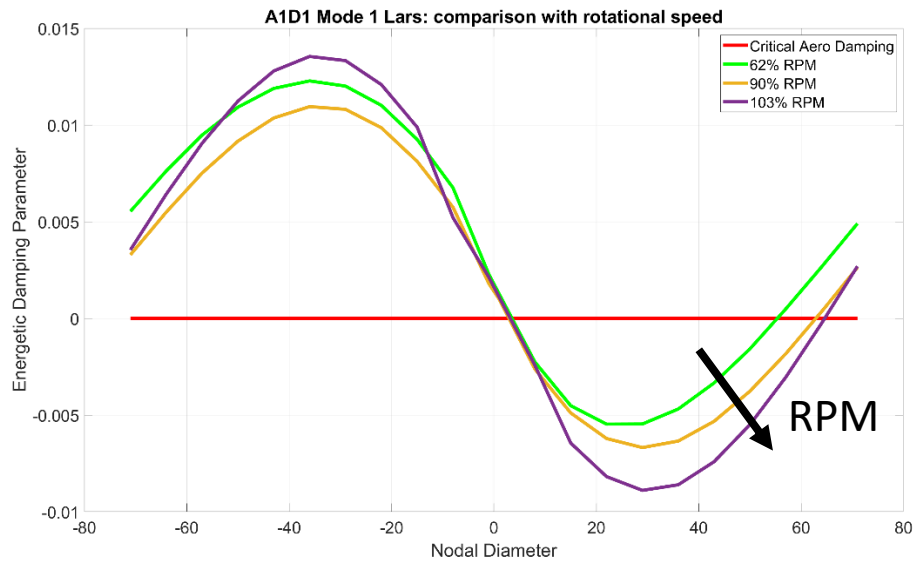


Figure 80: Aerodamping A1D1 Mode 1: Comparison with rotational speed



Figure 81: Aerodamping A1D1 Mode 2: Comparison with rotational speed

It's easy to see that there's an opposite behavior: while the first mode is destabilized increasing the rotational speed, the second mode is stabilizing increasing the rotational speed. This behaviour could alert the designers, because while they're trying to stabilize a mode, the other is destabilizing.

The first mode is stabilizing if the rotational speed decreases according with what has been said in Chapter 3: if the reduced velocity decreases, then the modeshape stabilizes.

The reason why the second mode stabilizes increasing the rotational speed is in the nature of that modeshape. In fact, as we said before, this mode tends to become a torsional mode increasing the nodal diameters. Decreasing the rotational speed also the incidence on the blade increases, so the blade becomes charger: in this way the nature of the modeshape could strongly interact with the major incidence and then the blade could extract more aerodynamic work from the fluid. The result is a destabilization of the mode.

4.4 Sensitivity around the configuration

In this chapter are presented the 3D flutter analysis on another ARIAS configuration, the A1SD, with which it's possible to analyze the influence of an under – platform steel damper on the level of flutter stability.

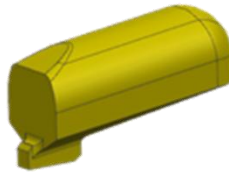


Figure 82: Under - platform steel damper

As done for the previous configuration, even in this case the damper is modelled as a “lumped mass”:

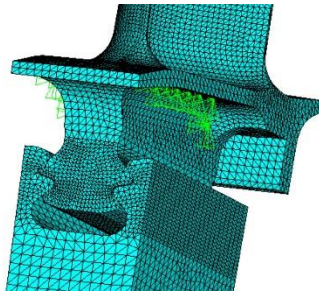


Figure 83: Damper FEM model

The CFD analysis are the same of the previous chapter, so there are not presented yet. For simplicity in this cases the analysis are mode only at 62 % of reference speed and at 103 % of reference speed, because these two operational point represent the extremes of the mission.

Let's now go to the 3D flutter analysis.

- **103 % of reference speed**

Here it is the FreND diagram:

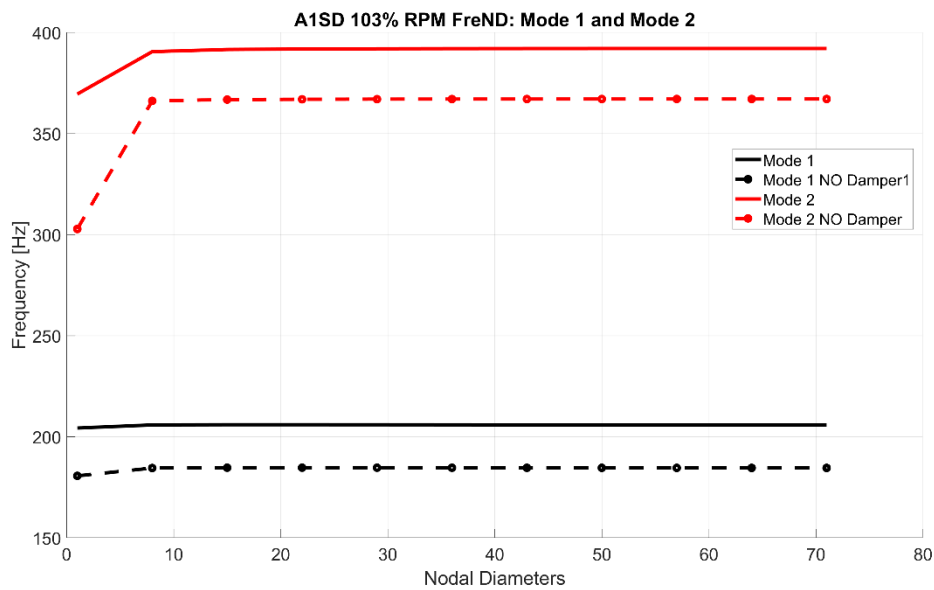


Figure 84: FreND A1SD: 103 % RPM

As expected with introduction of the steel damper the structure becomes stiffer: the natural frequencies increases.

Even in this case the numerical campaign is done using the linearized solver.

In the following page are presented the results for the Mode 1 and Mode 2.

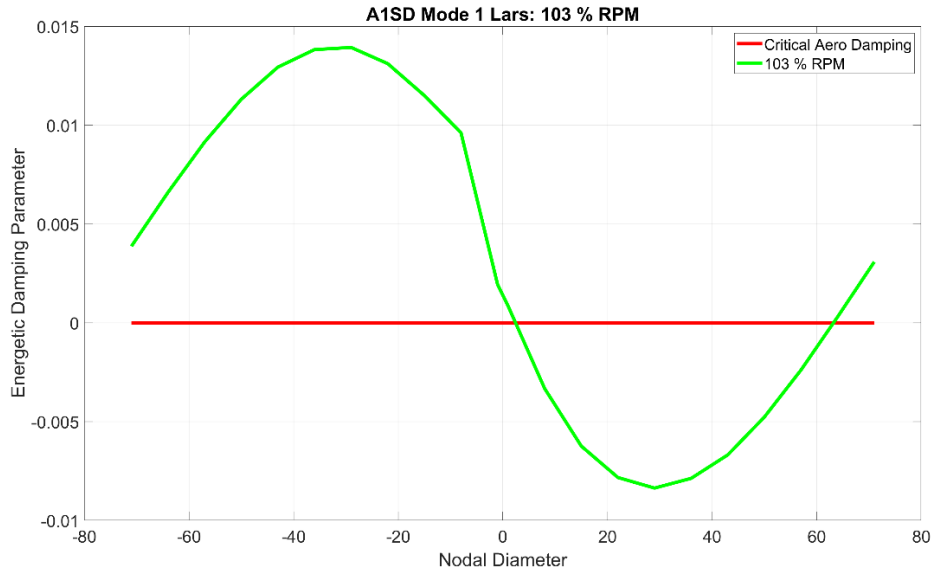


Figure 85: Aerodamping A1SD 103 % RPM: Mode 1

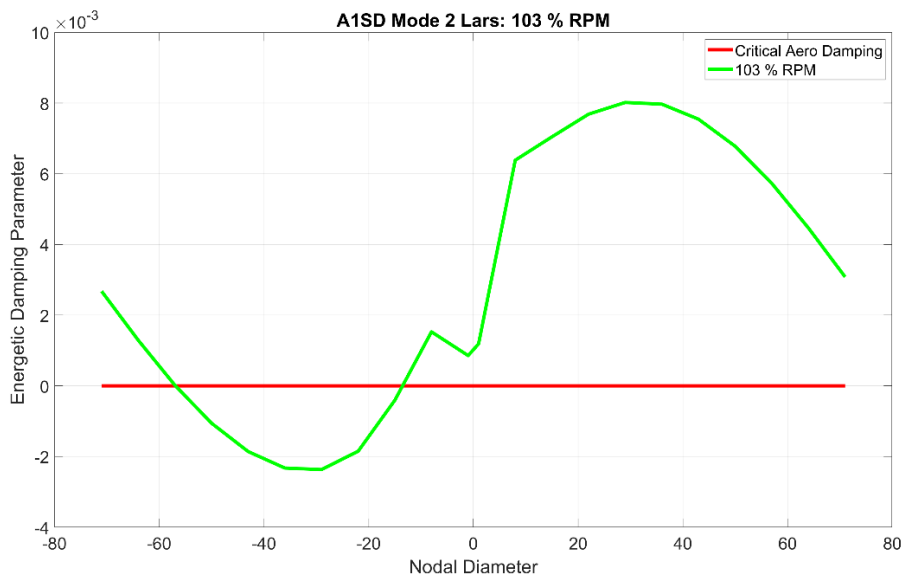


Figure 86: Aerodamping A1SD 103 % RPM: Mode 2

- **62 % of reference speed**

Now it's time to present the same analysis made at 62 % of reference speed.

As already said before, even in this case the introduction of the damper increases the stiffness of the structure.

In the next picture there is the FreND diagram:

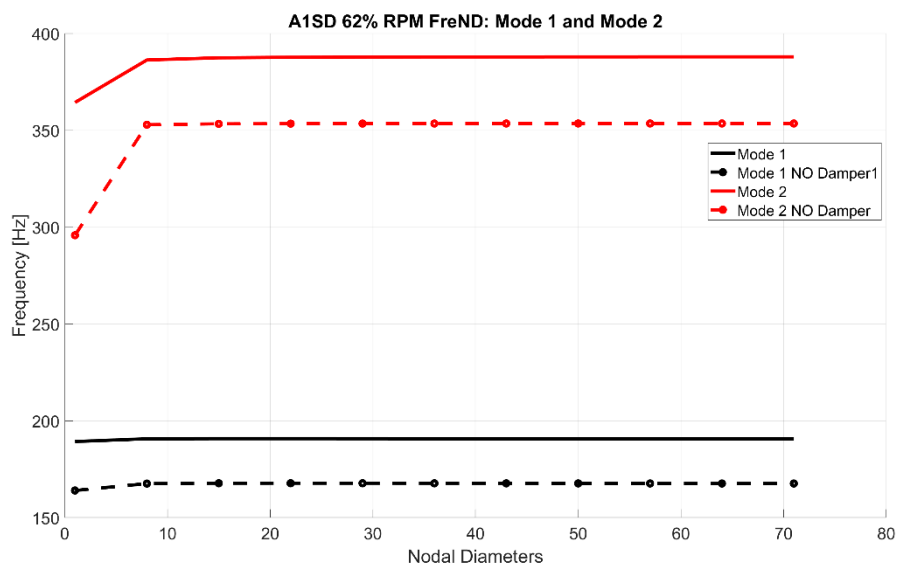


Figure 87: FreND A1SD: 62 % RPM

In the next page are presented the results of the analysis for Mode 1 and Mode 2.

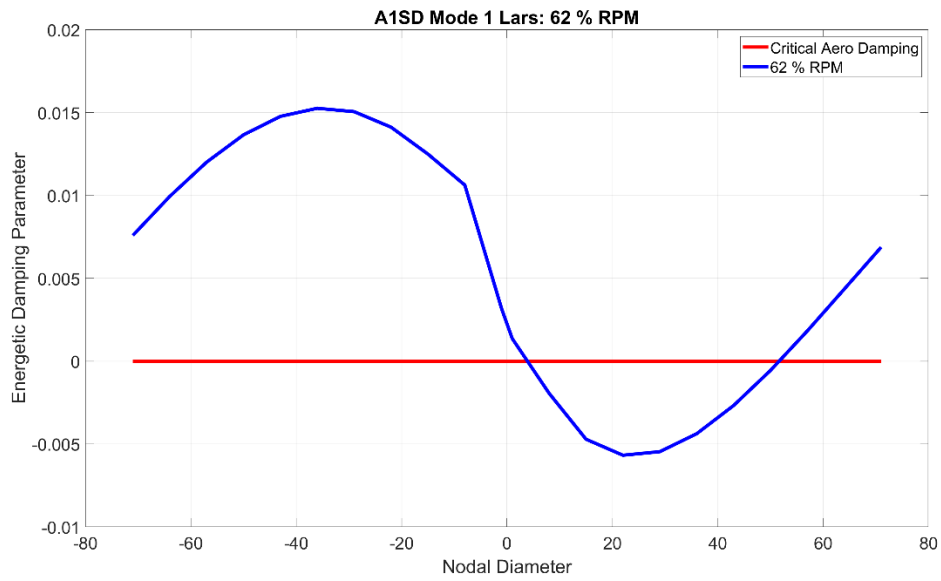


Figure 88: Aerodamping A1SD 62 % RPM: Mode 1

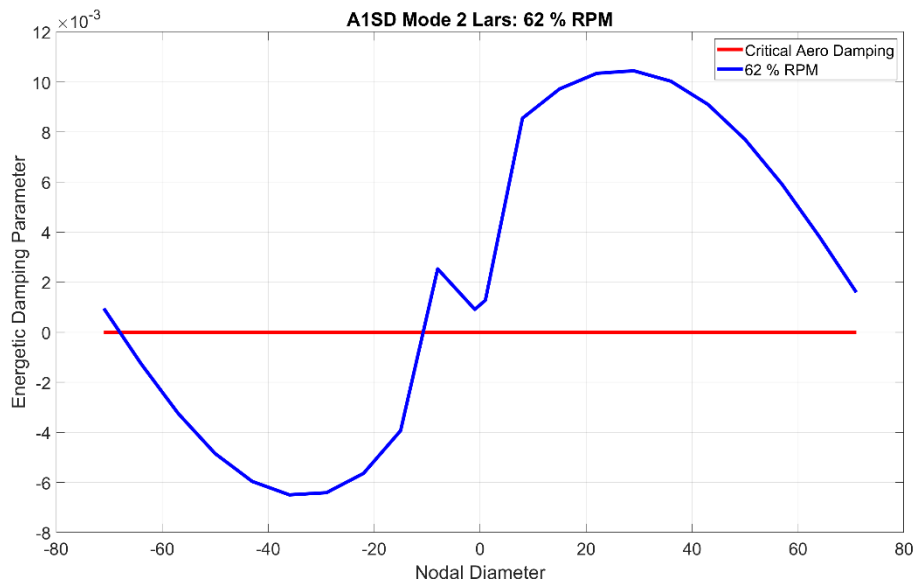


Figure 89: Aerodamping A1SD 62%: Mode 2

- **Comparison**

Let's now plot on a unique graphic, one for each mode, the results to see the effect of the rotational speed on the level of flutter stability.

For the Mode 1 we obtain:

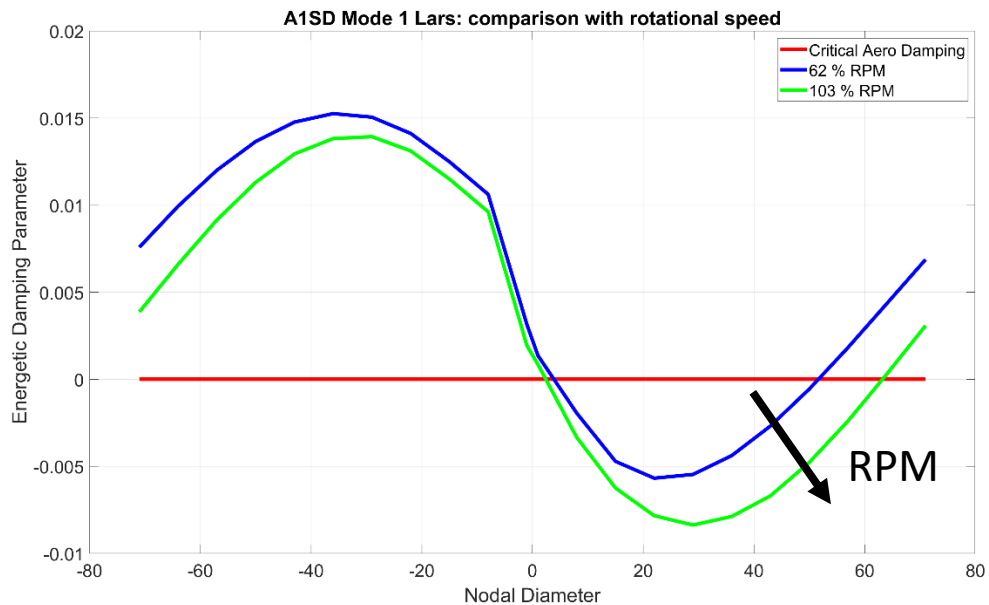


Figure 90: Aerodamping A1SD Mode 1: Comparison with rotational speed

This behavior does not create any problems: it is almost the same as the A1D1 configuration. Both the modes aren't stable and increasing the rotational speed destabilizes the modes. So the presence of the damper does not influence the modeshape's level of flutter stability.

Now let's go to the second mode. In this case, to evidence the influence of the damper on the modeshape, on the same graphic are plotted the same curves relative to the un-damped configuration.

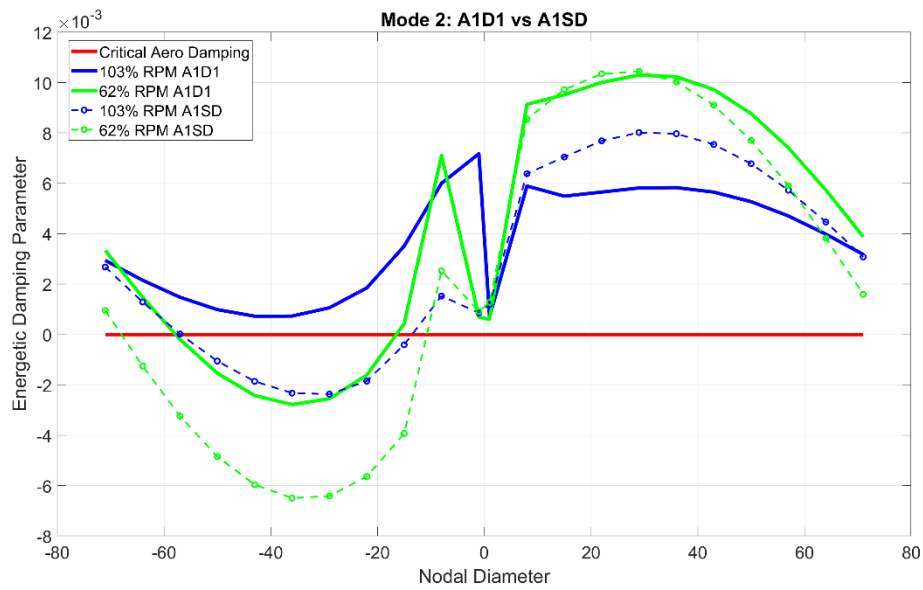


Figure 91: Aerodamping: A1D1 vs A1SD

This situation could alert the designers: the introduction of the damper, which is helpful for FRA (Forced Response Analysis) could strongly destabilize one mode of the blade. Both the curves (62 % RPM and 103 % RPM) are translated downward. So it is necessary to perform a dedicated 3D flutter analysis for the configuration with the damper.

For completeness it's possible to isolate the most critical nodal diameter, which in this case is the -36, and analyze the distribution of aerodynamic work on the blade's surface.

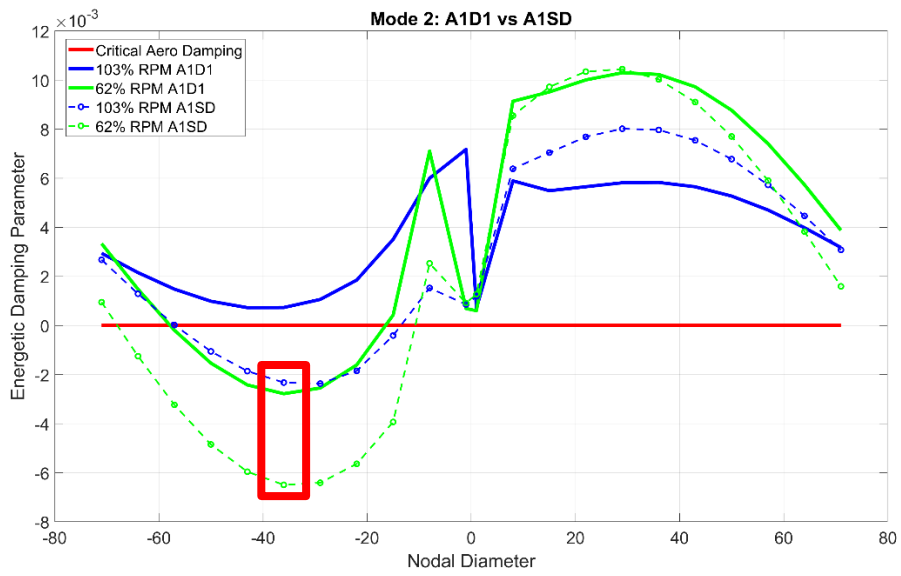


Figure 92: A1SD: Critical nodal diameter

From the solver's results in fact it's possible to extract the density of aerodynamic work on the blade's surface:

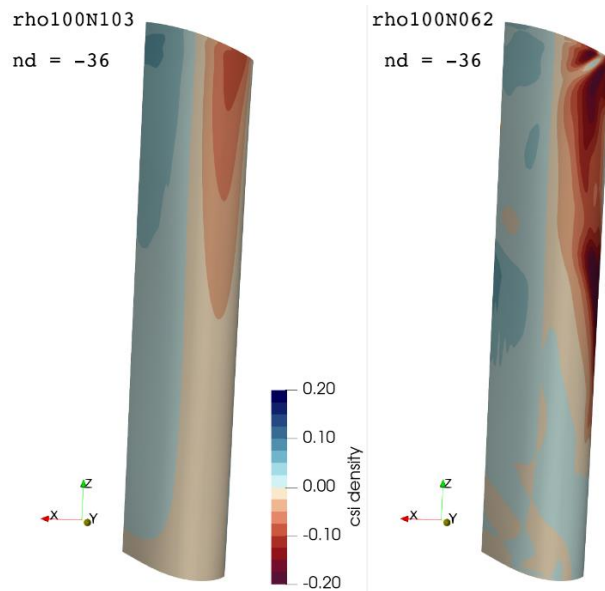


Figure 93: Density of aerodynamic work

So in this way is clearly explained why the Mode 2 is strongly more unstable at 62 % RPM, in fact from the previous picture is easily to see that in this operational point the blade extracts more aerodynamic work on the fluid. The surface integration of the density of the aerodynamic work is the point which is plotted in all the figures presented in all the analysis.

Lastly in the next chapter will be presented the sensitivity around the solvers.

4.5 Sensitivity around the solvers

In this chapter is presented the comparison of the results of 3D flutter analysis between the two solvers: the Linearized solver (LARS code) and the Non – linearized solver (TrafNL code).

For this numerical campaign is used again the A1D1 configuration and for simplicity in this case the results are presented only for Mode 2 at 62 % RPM and 103 % RPM.

First of all to better comprehend this analysis it's necessary to present the CFD field around the blade:

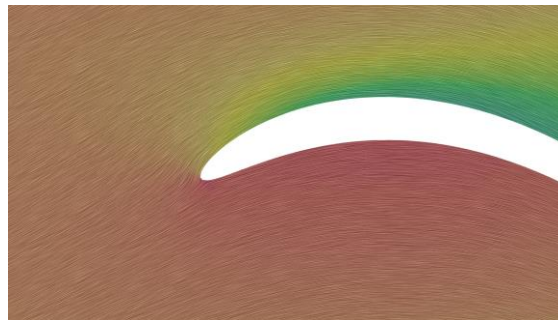


Figure 94: CFD analysis 103 % RPM: Pressure field

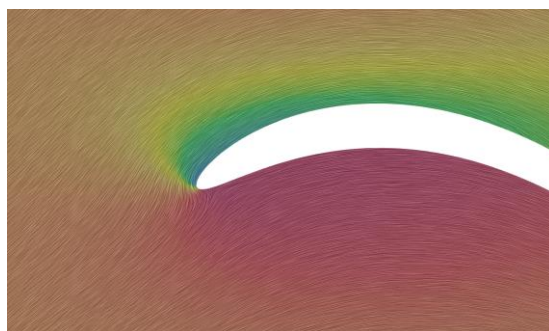


Figure 95: CFD analysis 62 % RPM: Pressure field

From these figures it's possible to view that at 62 % RPM the incidence on the blade increases. Then there's also a large separation region on the suction side of the profile. This is a non linear phenomenon: this fact will be very important in the next pages.

Now let's present the results of the 3D flutter analysis using the Non – Linearized solver. In the same graphic is also plotted the curve obtained with the linearized solver, in the way to better understand the possible differences between the two methods.

At 103 % we obtain:

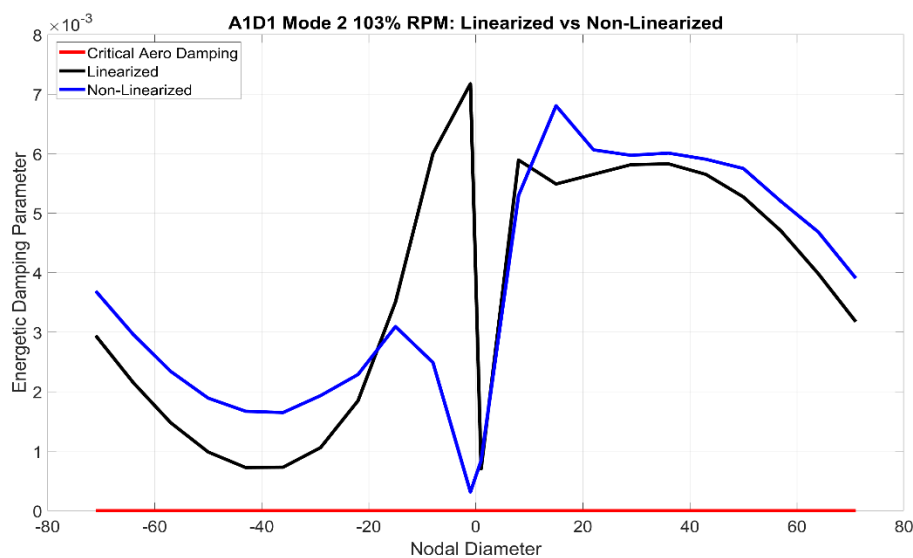


Figure 96: A1D1 Mode 2 103 % RPM: Linearized vs Non – Linearized

In this case it's possible to see that there aren't big difference between the results: this is an uncoupled method, so it's important the sign of aerodamping. The curves could be different between each other but the result is almost the same.

At 62 % RPM we obtain:

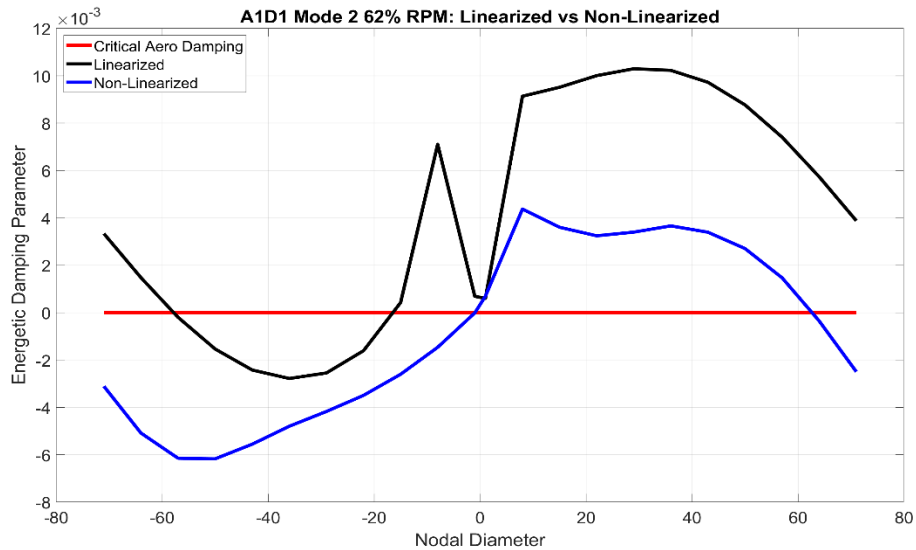


Figure 97: A1D1 Mode 2 62 % RPM: Linearized vs Non – Linearized

In this case the situation is different: when a non linear phenomenon (separation) is present the Non – Linearized solver is more reliable, in fact in this case the two curves shows different results.

So, in the Off – Design point when non linear phenomenon are present, the Non – Linearized solver is strongly suggested.

The drawback of this method is the time: the linearized solver in fact is faster, it saves about 55 % of simulation's time.

Chapter 5

Conclusions

After this long treatment and a lot of results presented, now it's time for conclusions:

- The operational point could influence in a different way the level of flutter stability of the modeshape: increasing the RPM could stabilize one mode and destabilize the other.
- The introduction of the damper, which is very helpful to limit the amplitude of the forced response, could strongly destabilize one modeshape: a dedicated 3D flutter analysis of the model of with the damper is necessary.
- The Linearized method is faster: almost 55 % of time saved respect to Non – Linear analysis (2 hours of simulation against 4.5).
- The Non – Linearized method is worthy suggested if Non – Linear phenomena appear on the blade.

5.1 Future developments

In this work were presented a lot of different sensitivities, as example that one in which the configuration is fixed and varies the operational point. Now one possible development could be to make the 3D flutter analysis on a mistuned row and the analyze how the operational point influences the level of flutter stability. A mistuned row is a row in which some blades have an additional mass at the tip, which change vibration properties of it.

In ARIAS 144 for example a possible way to mistune the row is to use pockets of 2 blades: one with the additional mass e one no. In this case there are 72 pockets of 2 blades each. This configuration in the ARIAS project is called A1C2 – A1, where C2 is the name of the additional mass.

Now the phase angle is not between every blade, but between the pockets of them: it is called IPPA (Inter Pocket Phase Angle).

As said before, the presence of the additional mass changes the vibration properties of the blade: so the flutter response may could not propagate to other blades and the row could be stable.

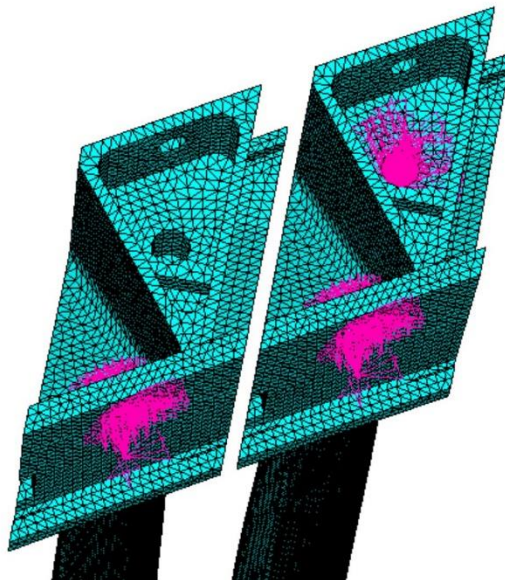


Figure 98: Double blade configuration

Here they are some examples of modeshape:

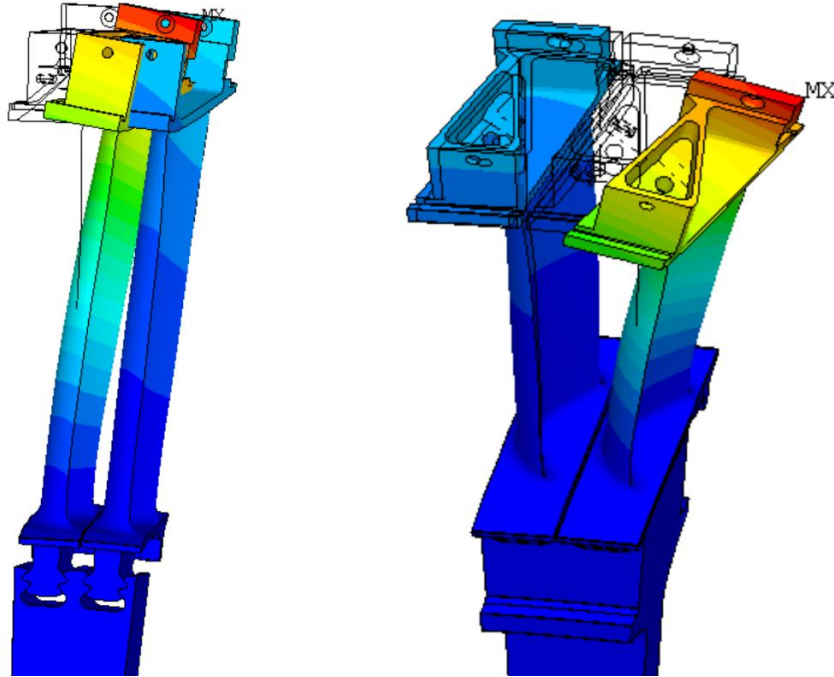


Figure 99: Mode 1 and Mode 2

In the next page it's possible to observe the results of 3D Flutter calculation at 62 % of RPM.

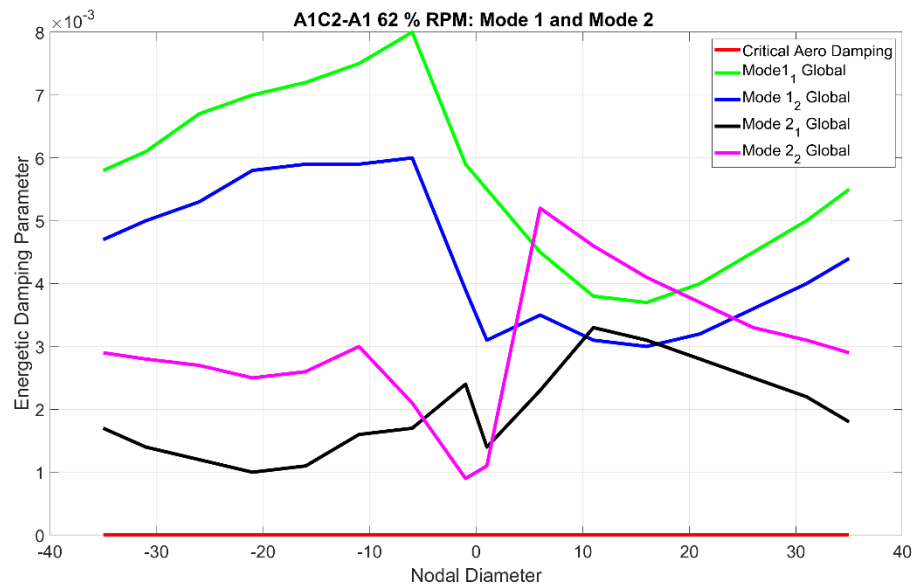


Figure 100: Aerodamping A1C2 - A1: Mode 1 and Mode 2

In this picture is possible to see the results at 62 % of reference speed: both modes are stable, while at the same speed were both unstable for the single blade configuration. So this type of mistuning is effectual. Now would be possible to study this configuration, or the 4 blades pocket configuration, changing the operational point of working, the solver ecc..

But this is another story!

References

- [1] Pinelli Lorenzo, Poli Francesco, Arnone Andrea, Schipani Claudia. (2009) *A time – accurate 3D Method for turbomachinery blade flutter analysis*, 12th International Symposium on Unsteady Aerodynamics.
- [2] F. Poli, E. Gambini, A. Arnone, C. Schipani, *A 3D time – linearized method for turbomachinery blade flutter analysis*.
- [3] F. Vanti, L. Pinelli, F. Poli, A. Arnone. (2017) *Aeroelastic investigation of turbine blade assemblies: cluster system and mistuned rows*, 12th European Conference on Turbomachinery Fluid Dynamics & Thermodynamics.
- [4] Lorenzo Pinelli. (2020) *Aeromechanics*, Università degli studi di Firenze.
- [5] Z. Mazur – Czerwicz, A. Hernández – Rossette, R. Garcia – Illesoas. (2006) *L – 0 blade flutter investigation of a 110 MW Geothermal Turbine*, ASME 2006 Power Conference.
- [6] Miroslav Pastor, Michal Binda, Tomas Harcarik. (2012) *Modal Assurance Criterion*, Elsevier Ltd. Selection.
- [7] Zucca Stefano, Botto Daniele. (2021) *Slides del corso “Dinamica dei rotori per applicazioni Aerospaziali”*, Politecnico di Torino.
- [8] Firrone Christian Maria. (2012) *Comportamento dinamico di ingranaggi per applicazioni aeronautiche*, Politecnico di Torino.

- [9] E – TDCs Abstract. (2023)
- [10] https://www.cfmaeroengines.com/wp-content/uploads/2021/07/CFM_RISE_Whitepaper_Media.pdf
- [11] https://www.cfmaeroengines.com/wp-content/uploads/2021/07/CFM_RISE_Whitepaper_Media.pdf
- [12] <https://aviationvoice.com/ge-aviation-completes-initial-ground-testing-of-ge9x-engine-2-201610201225/>
- [13] https://en.wikipedia.org/wiki/General_Electric_GE9X
- [14] https://en.wikipedia.org/wiki/General_Electric_T901
- [15] <https://www.defensenews.com/air/2019/02/02/general-electric-wins-517-million-contract-to-build-engines-for-armys-next-generation-helicopters/>
- [16] https://en.wikipedia.org/wiki/Brayton_cycle
- [17] <https://twitter.com/geadditive/status/1121061240678354946?lang=ar-x-fm>
- [18] https://en.wikipedia.org/wiki/General_Electric_Catalyst
- [19] https://it.wikipedia.org/wiki/File:Logo_Avio_Aero.jpg
- [20] <https://www.polito.it/>
- [21] https://www.researchgate.net/figure/Natural-frequencies-versus-number-of-nodal-diameters-for-the-tuned-rotor-by-finite_fig2_35686122
- [22] <https://www.parmadaily.it/7-novembre-1940-crollo-di-parte-del-tacoma-narrows-bridge/>
- [23] <https://www.unifi.it/>
- [24] <https://www.arias-project.eu>
- [25] https://www.cfmaeroengines.com/wp-content/uploads/2021/07/CFM_RISE_Whitepaper_Media.pdf